New insights into the structure and formation of coals, terrestrial and extraterrestrial kerogens from resonant UV Raman spectroscopy

Bruno Reynard, Eric Quirico, Lydie Bonal, Gilles Montagnac, Pierre Beck

New insights into the structure and formation of coals, terrestrial and extraterrestrial kerogens from resonant UV Raman spectroscopy.

Eric Quirico[1], Lydie Bonal[1], Gilles Montagnac[2], Pierre Beck[1] and Bruno Reynard[2]

[1]Université Grenoble Alpes, CNRS, Institut de Planétologie et Astrophysique de Grenoble (IPAG), UMR 5274, Grenoble F-38041, France

[2]Laboratoire de Géologie de Lyon, CNRS, Ecole Normale Supérieure de Lyon, 46 allée d'Italie – BP 7000, 69342 Lyon Cedex 07, France

16

17 **ABSTRACT**

18

19 Resonant UV (244 nm-excitation) Raman spectroscopy was used to characterize a series of
20 coals, type II kerogens, Insoluble Organic Matter (IOM) extracted from primitive chondrites
21 and two stratospheric Interplanetary Dust Particles. UV-Raman spectra of immature terrestrial
22 kerogens and coals are distinct from those of extraterrestrial kerogens extracted from type 1
23 and 2 primitive chondrites, allowing unambiguous identification. The degree of disorder in
24 the refractory carbonaceous matter in the considered IDPs is found to be higher than in
25 primitive chondrites, confirming former interpretation of visible (514 nm-excitation) Raman
26 spectra of IDPs. Spectral and structural features of laboratory analogues of chondritic organic
27 matter formed in cold plasma reactors at 500-700 °C differ from those of natural samples,
28 challenging the hypothesis that chondritic organic matter within the protosolar disk may form
29 through plasma reactions. Finally, UV Raman data shed new light in the structural evolution
30 of coals during maturation and support the presence of an sp^2 structural transition at vitrinite
31 reflectance Ro ~ 0.4-0.5%. Comparison with former visible Raman and infrared spectroscopic
32 data confirms the existence of this structural transition, which is related to a dramatic drop of
33 oxygenated species (carboxyl, hydroxyl, ketone and ether groups). Oxygen thus plays an
34 indirect but significant role in the control of the Raman spectra of polyaromatic materials. A
35 potential application of this technique is the determination of the biotic versus abiotic origin
36 of kerogens in ancient rocks on Earth, and of soils and rocks on Mars that is otherwise
37 difficult with classical visible-excitation Raman spectroscopy.

38

39

1. INTRODUCTION

On Earth, kerogens and coals are formed by the slow thermal degradation of living organisms. Their structure, at least in the first stages of their maturation, retains a memory of the polyaromatic structure and composition of their precursors (Van Krevelen, 1993; Vandenbroucke and Largeau, 2007). Extraterrestrial kerogens recovered from primitive chondrites were formed in local interstellar medium (ISM) or the protosolar disk through abiotic processes. There is no consensus to date on their formation process (Alexander et al., 2017). Their elemental composition is close to that of type III terrestrial kerogens, but their structure and composition is different. In particular, their polyaromatic structure is based on highly substituted polyaromatic units (1-4 rings) connected through a ramified aliphatic linkage with short alkyl chains (Cody and Alexander, 2005; Cody et al., 2002; Gardinier et al., 2000; Remusat et al., 2005a, 2005b; Wang et al., 2005), while in type III kerogens and coals the aliphatic linkage is made of longer chains, and overall the structure is less cross-linked (Vandenbroucke and Largeau, 2007).

Unravelling the biogenic versus abiotic origin of kerogens is a key issue in several fields of research. The search of ancient Life on Mars relies on investigations on Martian meteorites that host tiny refractory carbon inclusions, and in-situ analyses of the Martian soil and rocks at the surface or in the close subsurface by space missions (Steele et al., 2016, 2018). The surface of Mars is possibly inseminated by chondritic organic matter, due to meteoritic and micrometeoritic impacts (Quirico and Bonal, 2019). In this context, distinguishing chondritic kerogens from putative kerogens issued from a past Martian Life is a major challenge. A similar issue exists in the interpretation of ancient terrestrial kerogens (> 2 Gyrs), complicated in that case by the effects of severe thermal metamorphism (Bower et al., 2013; Foucher, 2019).

Raman spectroscopy, a versatile technique well suited to characterize solid natural samples, provides insights into the composition and structure of organic materials (Quirico and Bonal, 2019). The combined characterization of minerals and molecular species offers a valuable opportunity to investigate mineral-organic associations at the micrometric scale in metamorphic and sedimentary rocks, soils, sedimentary organic matter, meteorites and cometary dusts. Raman spectroscopy has been widely used in the laboratory for mineral and natural material identification, and is now available as portable instruments allowing field measurements. This includes two Raman instruments implemented aboard the Mars 2020 rover, which will investigate rocks and soils on the Mars planet: SuperCam, whose Raman sub-instrument operates at 532 nm and is designed to analyze targets as far as 14 m; and SHERLOC (Scanning Habitable Environments with Raman and Luminescence for Organics and Chemicals), holding a Raman sub-instrument operating with a UV 248.6 nm excitation at a spatial resolution of 50 µm (Beegle et al., 2020; Wiens et al., 2016).

Raman spectroscopy has been widely used to characterize the maturation grade of coals and kerogens, complementing the usual ranking method based on reflectance measurements (Jehlička et al., 2003; Kelemen and Fang, 2001; Quirico et al., 2005a; Wopenka and Pasteris, 1993), and to implement carbon thermometers (Beyssac et al., 2002; Lahfid et al., 2010). The structure of carbonaceous matter as determined by Raman spectra is also influenced by other parameters, such as the nature of the precursor, pressure, oxidation reactions, and kinetics in the case of short duration thermal events (Bonal et al., 2016; Quirico et al., 2009, 2018). For instance, terrestrial coals and extraterrestrial kerogens hosted by primitive chondrites display significant differences in their first-order carbon bands collected with a 514 nm excitation, which may be due to a precursor effect or post-accretional parent bodies conditions (Quirico et al., 2009). Disentangling the respective contribution of these processes is a difficult yet essential step in making Raman spectroscopy a quantitative tool for

89 assessing the conditions of formation and precursors of carbonaceous matter in ancient
90 terrestrial and extraterrestrial settings.

91 Raman spectroscopy that uses excitation in the deep UV (200-250 nm) has been
92 shown to present advantages over classical Raman spectroscopy that uses excitation in the
93 visible to near IR range. UV-Raman spectra are generally devoid of fluorescence, and a
94 certain number of species have resonant transitions enhancing their detection limit (Asher,
95 1993). Drawbacks have also been identified, such as sample damage due to photolysis or
96 annealing, and low scattering yield due to a weak penetration of UV photons. We report a 244
97 nm Raman survey of a series of terrestrial sedimentary organic matter samples that includes
98 coals and three type II kerogens, covering a broad range of maturities. Only few UV Raman
99 spectra have been published so far on sedimentary organic matter, and these data should be
100 helpful in the context of the study of carbonaceous matter in ancient rocks on Earth,
101 meteorites and the Mars 2020 mission. We also report new Raman spectra of Insoluble
102 Organic Matter (IOM) extracted from the Renazzo (CR) and Murray (CM) primitive
103 chondrites, along with spectra of IOMs and stratospheric IDPs published earlier (Dobrica et
104 al., 2011; Quirico et al., 2014). We first address technical aspects on the implementation of
105 244 nm Raman spectroscopy. Then, we report new insights into the structure of these
106 terrestrial and extraterrestrial kerogens, and discuss fours issues: (1) distinguishing terrestrial
107 biogenic kerogens from abiotic chondritic kerogens; (2) the structure of carbonaceous matter
108 in IDPs compared to chondrites; (3) the putative formation of chondritic kerogen by plasma
109 reactions and (4) the investigation of coal maturity and the role of oxygen in the Raman
110 signature.
111

112 **2. MATERIALS AND METHODS**
113

114 *2.1 Samples*

115 Coal samples were provided by the Penn State data bank (Table 1). Their maturity is
116 rated by their mean maximum vitrinite reflectance (Ro, %), and their elemental ratio H/C and
117 O/C are also provided. Type II kerogens were provided by Institut Français du Pétrole (Rueil-
118 Malmaison France; courtesy of Mrs M. Vandenbroucke). They were recovered from different
119 Toarcian wells and outcrops: MENIL/VAIR, outcrop (K99296); DICKEL4, 1416 m (K20505)
120 and REHDEN9, 1306 m (K20507). The H/C and O/C elemental ratios were also provided, as
121 well as the Ro reflectance of allochthonous vitrinite for K20507 and K20505. Allochtonous
122 vitrinite is not a fully reliable tracer, because its diagenetic history before incorporation into
123 the type II kerogen is unknown. For K20505 with respect to K20507, the vitrinite reflectance
124 of 0.57 and 1.25 %, respectively, are consistent with the H/C values of 1.09 and 0.80,
125 respectively. As K99296 is obviously more immature than the two other kerogens
126 (H/C=1.23), the maturity of these samples is as following: K20507>K20505>K99296.

127 Chondrites were supplied by the Muséum National d'Histoire Naturelle (MNHN -
128 Paris, France). Stratospheric IDPs, L2008x3 and W7013I1, were supplied by the NASA-
129 Johnson Space Center, and were earlier characterized by 514 nm Raman spectroscopy (Bonal
130 et al., 2011). The 244 nm Raman spectra of L2008x3 were presented in Dobrica et al. (2011)
131 but not quantitatively analyzed.

132 IOM samples from Renazzo and Murray were extracted following two methods.
133 Murray IOM was obtained through protocol very similar to the one described in Gardinier et
134 al. (2000) and adapted to ~100 mg samples. The sample was ground by hand with a pillar and
135 mortar, and ~100 mg was introduced into a polypropylene micro-tube. A first step consisted
136 in the elimination of soluble compounds through: (i) washing in distilled water V(H_2O)= 1
137 ml, 15 min sonication, centrifugation (30 min 6000 rpm), supernatant removal; followed by
138 (ii) washing in 0.5 ml CH_2Cl_2:CH_3OH (v/v=1/2), 30 min stirring, centrifugation and

supernatant removal. The second step consisted in eliminating carbonates: 37% HCl, V(HCl)=V(H_2O)=0.75 ml. Sonication for 1 h. Neutralization of the solid residue by addition of distilled water until getting a 6-7 pH. The third step had for objective the dissolution of silicates: HCl (37%) and HF (48%), V(HF) = 2V(HCl/H_2O = 1/1) = 0.5 ml, 8 h sonication and N_2 bubbling, centrifugation and neutralization, operation executed three times. The fourth step consisted in the elimination of neoformed minerals (fluorures): V(HCl) = V(H_2O)=0.75 ml, 80°C 1 h sonication, repeated 2-3 times. The fifth and last step was similar to the second step, for removing encaged soluble molecules.

Renazzo IOM was obtained with a protocol dedicated to very small amount of sample. Around ten grains of 100-500 µm of maximum dimension were deposited on an Au foil with curved edges in order to prevent grain loss. The foil was then inserted in a Teflon holder, placed in an alumina box covered with a polycarbonate window, which allowed a visual control of operations with a binocular microscope (Fig. 1a). Inside the reactor, liquids were simultaneously injected and expelled with a peristaltic pump (90.5 µl.min^{-1}). Viton® tube were used to carry the liquids, and were hold inside the reactors by two micromanipulators (Fig. 1b). The reactor was continuously purged with gaseous nitrogen or argon to ensure a non-oxidizing atmosphere, and to minimize micromanipulators etching. The chemical procedure was similar to that previously described, except the lack of sonication or mechanical stirring. Demineralized grains were then recovered from the gold foil, and transferred on glass slides for Raman analysis (Fig. 1c). The present protocol has been validated by comparing etched µm-sized matrix grains, with IOM extracted with the standard procedure dedicated to macroscopic samples. In both cases, a significant enrichment in carbon was observed through energy dispersive X-ray spectrometry in a scanning electron microscope, but with a variety of sulfides that survived the acid attack (detection of S and Fe).

164 *2.2 Raman spectroscopy*

165 Spectra were collected with a JOBIN-YVON-Horiba LabRam system with a
166 frequency-doubled Ar^+(244 nm) excitation and a microscope equipped with an OFR™ 40×
167 objective with a 240-360 nm broad band transmission (> 80%). (Laboratoire de Géologie de
168 Lyon Terre, Planètes, Environnement/ENS-Lyon France). The laser spot on the sample had a
169 diameter of 3–5 micrometers. Two gratings were used, 3600 and 600 gr/mm, that allow
170 covering spectral ranges of 400-1500 and 400-3500 cm^{-1}, respectively. In the case of
171 immature coals (Ro < 1%) and type II kerogens, IOM samples and IDPs, the laser power
172 delivered to the sample was fixed to 300 µW. For most of the measurements, the acquisition
173 time was 2x150 s and the 600 gr/mm grating was used. When seeking for faint narrow
174 spectral features (see below), the acquisition time was increased up to 4x300 s, and both
175 gratings were used. The mature coals with Ro>1% were measured with a laser power of ~500
176 µW, acquisition time of 2x300 s and a 3600 gr/mm grating.

177 Sample stability under 244 nm laser irradiation is a critical issue. Photochemical or
178 thermal damages can be induced by the focused laser beam, depending on the power
179 deposited on the sample and on its fragility. The presence of a crater or color modification at
180 the laser spot was visually inspected for each measurement. Measurement conditions (i.e.
181 laser power, collection time) were optimized through time-resolved measurements at the same
182 spot location (see Appendix). Tests were run in air and under argon atmosphere by means of
183 an environmental cell. Using an inert atmosphere reduces photo-oxidation, which causes
184 possible fluorescence and evolution of the Raman spectra with time. The gain was however
185 too small compared to signal loss through the cell window, and spectra were mostly collected
186 in air. Because laser-induced damages can be almost instantaneous, we also investigated the
187 effect of exposure time on a coal sample by using a rotating sample holder. We found no
188 spectral difference with measurements performed under static conditions. In contrast, similar

measurements under static and rotating conditions on a cellulose sample revealed dramatic spectral modification reflecting alteration of the sample for both conditions. Coal samples are probably more resistant because they underwent metamorphism during burial in the sediment pile or due to tectonic events, and their most fragile and thermally labile fraction was expelled or transformed during thermal maturation. However, even for mature coals and kerogens, a limited photochemical or thermal alteration cannot be ruled out.

The raw UV-Raman spectra of terrestrial an extraterrestrial kerogens are available in the GhoSST/SSHADE spectral database (Quirico, Eric; Montagnac, Gilles (2006a,b)).

The Raman spectra were corrected with a linear baseline between 830 and 1925 cm^{-1}. The Raman G- and D-carbon bands were fitted with the so-called Lorentzian-Breit-Wigner-Fano (LBWF) spectral model following Ferrari and Robertson (2000) (Fig. 2):

$$I(\omega) = I_G \frac{[1 + 2(\omega - \omega_G)/Q.FWHM_G]^2}{1 + [2(\omega - \omega_G)/FWHM_G]^2} + \frac{I_D}{1 + 4(\omega - \omega_D)^2/FWHM_D^2}$$

where ω_G and ω_D are the resonant frequencies (in cm^{-1}) of the G and D bands, I_G and I_D their peak intensity, $FWHM_D$ and $FWHM_G$ their full width at half maximum, and Q the coupling coefficient. The fit finally provided, for each sample, $FWHM_D$, $FWHM_G$, ω_G and ω_D, as well as the ratios of peak intensities (I_D/I_G) and integrated intensities ($A_{DDG}=A_D/[A_D+A_G]$). Note that the peak position of the G band does not correspond to the ω_G, and is equal to $\omega_G+FWHM_G/2Q$.

For the sake of comparison with former studies (Quirico et al. (2014) and Kuga et al. (2015)) that used a slightly different (with or without constant) LBWF fit, the Raman spectra from Quirico et al. (2014) have been reanalyzed and the Raman parameters of Kuga et al. (2015) have been rescaled by applying a correction factor. These earlier studies used similar experimental conditions as those used here – 300 µW on the sample, 40x objective and 600

g/mm grating -, making the comparison possible.

The electronic data collected in this study can be freely downloaded from the SSHADE/GHOST spectroscopic database (https://www.sshade.eu/), at https://doi.org/10.26302/SSHADE/EXPERIMENT_LB_20200414_001

3. RESULTS

3.1 Coal and kerogen samples

Raman spectra obtained with 244-nm excitation are different from those collected with a visible excitation (Fig. 3). This wavelength dependence is due to the resonant process, i.e. the excitation photon is absorbed before being inelastically scattered. Different photon energies then lead to probing different fraction of the carbonaceous material (Merlen et al., 2017). Spectra of immature samples are devoid of the fluorescence background that occurs with visible excitation, and display an intense and sharp G-band (centred at 1600-1610 cm^{-1}), accompanied by a broad D band centred at 1360-1440 cm^{-1}, weaker in intensity with respect to the G band by a factor of ~ 2-5. A weak feature at ~ 1750 cm^{-1} appears as a shoulder of the G band, along with other weak and narrow substructures in the D band at ~ 1190, 1280 and 1450 cm^{-1} (Figs. 3, 4). Spectral variations with vitrinite reflectance are subtle in the range 0.3-2 % Ro and become more significant above this value (Figs. 4,5). The LBWF fit parameters, $FWHM_G$, ω_D, I_D/I_G and A_{DDG} fairly correlate with the vitrinite reflectance for values larger than ~ 1 % R_O (Fig. 6; Table 2). In contrast, the peak position of the G band and the width of the D band are nearly insensitive to maturity variations in the range Ro= 1 to ~3%. Only the anthracite sample with the highest maturity shows a clear modification of ω_G and $FWHM_D$. In the range 0.3-0.8 % R_O, $FWHM_D$, $FWHM_G$ and A_{DDG} vary strongly between 0.3 % R_O and

237 0.5 % Ro and become stable above this value (Fig. 7). In contrast, I_D/I_G, ω_G and ω_D do not
238 show systematic variation with the vitrinite reflectance in the range 0.3 -0.8%.

239 The spectra of type II kerogens are similar to those of coals (Fig. 5), and do not
240 present the strong fluorescence that prevents the detection of Raman features in spectra
241 collected with a 514 nm excitation. At first inspection, the UV Raman spectra of three
242 kerogen samples are identical. However, fitted parameters reveal significant differences
243 between these samples (Fig. 8), with a low I_D/I_G ratio (Fig. 8a) for K20507 and distinct values
244 of $FWHM_G$ and ω_G among the three samples (K20507, K99296 and K20505, with H/C= 0.80,
245 1.23 and 1.09, respectively). In these diagrams, kerogens K99296 and K20505 are very close
246 to the more mature coals (Ro=0.52 and 0.73%).

247

248 *3.2 IOM and IDPs*

249 244 nm Raman spectra with good signal-to-noise ratio could not be obtained from raw
250 matrix fragments of chondrites, due to the small penetration of incoming UV photons in the
251 sample (Fig. 9). Therefore, matrix fragments were treated through a HF/HCl acid attack prior
252 to UV-Raman measurements. At first sight, the spectra share similarities with those of coals
253 and kerogens (Fig. 10). They display an intense and narrow G band, and a weaker and broader
254 D band. A weak feature at 1750 cm^{-1} is sometimes observed. The second-order carbon bands
255 (2500-3500 cm^{-1}) could be observed, but they did not provide additional information to those
256 of the first-order G and D bands. Besides first-order similarities, a major spectral difference
257 between coal and kerogens and extraterrestrial samples is the shape of the D band. The D-
258 band looks like a shoulder of the G-band in IOM spectra (Fig. 11d), and the minimum
259 between the D- and G-bands is much fainter in IOM than in coals. Raman parameters I_D/I_G
260 (Fig. 11a) and ω_G (Fig. 11b) are, with a few exceptions, lower in chondrites than in coals. On
261 the other hand, type II kerogens plot along with chondrites and coals. Overall, coals, kerogens

262 and chondrites display similar $FWHM_G$. The ω_D parameter unambiguously distinguishes
263 extraterrestrial materials and coals, and type II kerogens display values across those two
264 groups. The A_{DDG} parameter efficiently discriminates extraterrestrial and terrestrial samples
265 (Fig. 11c).

266 UV-Raman spectra were collected on two stratospheric IDPs: L2008X3 and W7013I1,
267 and were partly published in Dobrică et al. (2011) (Fig. 12). Due to the small size of those
268 particles, no HF/HCl acid attack was attempted. The signal-to-noise ratio of L2008X3 spectra
269 is similar to that of IOM extracted from chondrites, but it is too low in W7013I1 to attempt
270 spectral fitting. In the latter sample, the peaks at 800-840 cm^{-1} are attributed to iron-rich
271 olivine. Accordingly, we infer that the abundance of polyaromatic organic matter is higher in
272 L2008X3. The IDP L2008X3 displays a much higher value of $FWHM_G$ and much lower
273 value of ω_G than chondrites, coals and kerogens (Fig. 11a).

274 The insert in figure 12 shows raw and smoothed spectra in the range 1900-2400 cm^{-1},
275 pointing to faint features at 2220 and 2325 cm^{-1}. These features, unobserved in 514 nm
276 Raman spectra, are likely resonant with a UV excitation wavelength. The band at 2320 cm^{-1}
277 corresponds to the stretching vibration mode of the N_2 molecule whose nature, atmospheric
278 versus adsorbed on the sample (Smudde et al., 1995) cannot be resolved due to the low signal-
279 to-noise ratio. The atmospheric O_2 stretching vibration modes at ~ 1550 cm^{-1} was not detected
280 due to the merging with the carbon G band. The weak feature at 2220 cm^{-1} is likely due to the
281 cyanide –CN functional group, as proposed by Quirico et al., (2008a). Indeed, no other
282 organic functional group is plausible in the range 2200-2250 cm^{-1}, and this band has already
283 been confidently identified by 244 nm Raman spectroscopy in heated N-rich tholins (Bonnet
284 et al., 2015). Cyanide groups have been identified in N-rich Ultra-Carbonaceous Antarctic
285 Micro-Meteorites (UCAMMs) (Dartois et al., 2013), and tentatively detected in Orgueil IOM
286 by Nuclear Magnetic Resonance (NMR) spectroscopy (Remusat et al., 2005b). The –CN

functional group is known to be thermally labile. Its presence in L2008X3 and absence in most chondritic IOMs (except possibly Alais), support the view that refractory organics in this IDP were less thermally processed.

4. DISCUSSION

4.1 Coal and kerogens maturity

In the range Ro=0.3-1%, several fitted Raman band parameters show a large evolution below 0.5% and constant values above (Fig. 7). In Raman spectra acquired with a 514 nm excitation, a linear correlation between $FWHM_G$ and ω_G is reported for immature coals (Quirico et al., 2003). Looking back in detail this old dataset, we observe that the data points cluster into three groups in a FWHMG vs. ω_G diagram: R_O < 0.4%, 0.4 <R_O (%) <1 and R_O > 1% (Fig. 13). It suggests the existence of a small but significant change of the polyaromatic structure of coals at Ro ~ 0.4 %, and points to a significant evolution above 1 Ro%. Thus in the maturity range Ro < 1%, coals clearly experience a chemical evolution (modifications of H/C and O/C, Table 1), but also some structural modifications. This point is consistent with the infrared spectroscopic measurements of Chen et al. (2012) that show that coals with Ro < 1.5 % experience a progressive aromatization. They also show that the size of the polyaromatic units (i.e. the degree of aromatic condensation) increases with increasing Ro in the range 0.4-2 %, while no significant variations are observed for Ro < 0.4 %. The number and diversity of oxygenated functions also show a dramatic drop above R_0 ~ 0.4 - 0.5 % (Petersen et al., 2008). This includes carboxylic, ketone, hydroxyl (essentially phenolic), quinone and ether groups. Raman spectroscopy probes the sp^2 structure of carbonaceous material (Ferrari and Robertson, 2000), which in coals is essentially present as aromatic and polyaromatic units (Van Krevelen, 1993). Phenol and quinone groups are part of the

polyaromatic structure, and ether groups may also be involved when bridging polyaromatic units. In the case of very disordered carbonaceous materials, the parameters that control the Raman spectra are not only the size of their very small aromatic units, but also the molecular environment of those units (e.g. degree of substitution, nature of the branched species) (Ferrari and Robertson, 2000). It results in a complex control of the first order carbon bands, and sometimes in a degeneracy issue as different carbonaceous materials may exhibit similar spectra at a given excitation wavelength (Ferrari and Robertson, 2001). In the case of immature coals, we think it is premature to decipher between polyaromatic units size and oxygen speciation as controlling parameters of the Raman spectra. Both parameters most likely play a role. In conclusion, the analysis of spectra acquired at both 244 and 514 nm laser wavelength supports the view that significant structural changes happen in coals at Ro~0.4 %.

In the range R_O > 1%, the $FWHM_G$ and ω_D parameters, and to a lesser extent I_D/I_G and A_{DDG} (data points around Ro ~ 2 % are more scattered), correlate well with the vitrinite reflectance (Fig. 6). These results are consistent with those obtained with a 514 nm excitation, in the case of the $FWHM_G$, ω_D, I_D/I_G and A_{DDG} parameters (Quirico et al., 2005a). $FWHM_D$ and ω_G provide no significant information, except that the anthracite sample is clearly different from other coals (Fig. 6). The ω_G is found poorly useful with either the 244 or 514 nm excitations. $FWHM_D$, which is a very sensitive and powerful maturity tracer of spectra acquired at 514 nm, is useless with a 244 nm excitation, in this maturity range at least. The 244 nm excitation efficiently traces maturity for Ro > 1%. The main parameter that controls the Raman spectra is likely the size of the aromatic units. Above Ro ~ 0.5%, a sharp decrease of elemental oxygen (i.e., oxygenated groups) is observed (Table 1), leading to a low oxygen concentration at Ro > 1% (O/C < 0.04). Only hydroxyl and ether groups remain in the structure, with variable concentration ratio from one coal to another (Petersen et al., 2008).

336 The UV-Raman spectra of the three kerogens K99296, K20505 and K20507 are close
337 to those of immature coals. The 244 nm excitation presents a clear advantage for these
338 samples as no 514 nm Raman spectra could be collected on K99296 and K20505 due to high
339 fluorescence that is absent with UV excitation. In the graphics $FWHM_D$ vs. I_D/I_G and
340 $FWHM_G$ vs. ω_G (Fig. 8), the more mature kerogen K99296 (with H/C = 0.80) plots apart the
341 other samples. K20505 and K20507 plot at the edge of the area defined by immature coals in
342 both graphs. The maturity of K20505 and K20507 is rated by allochthonous vitrinite mean
343 maximum reflectance Ro, 0.57 and 1.25 %, respectively (Table 1). These two samples do not
344 plot with coals that have similar Ro values (Fig. 8), pointing to a possible precursor effect as
345 type II kerogens and coals originate from different marine (planktonic) and continental
346 (higher ligno-cellulosic plants) environments. However, caution should be used when using
347 allochtonous vitrinite reflectance. As their prior history before incorporation into the kerogen
348 in unknown, they may not properly trace the actual thermal history of the kerogen. In
349 addition, maturation happens in an open system in the sediments in the case of kerogens, and
350 a rather closed environment in the case of coals. The carbonization processes may thus play a
351 role in shaping the different structure and chemistry and coals and kerogens.
352
353 *4.2 Insoluble organic Matter in Chondrites and IDPs*
354 The 244 nm Raman parameters of chondritic IOMs evidence little difference between
355 IOM of the studied carbonaceous chondrites (Fig. 11). I_D/I_G may point to a possible
356 distinction of Murchison/Orgueil/Ivuna from Tagish Lake (heated lithology), as previously
357 suggested by Quirico et al. (2014). However, they do not confirm the distinction with Cold
358 Bokkeveld, a CM that experienced a mild heating event (Quirico et al., 2018). Murray (CM)
359 displays a low $FWHM_D$ value, and the primitive CR Renazzo plots close to Tagish Lake.
360 $FWHM_D$ and I_D/I_G do not clearly discriminate chondrites having experienced mild heating

events, and the other parameters do not provide further information. Structural differences are faint and unconstrained by UV Raman spectroscopy. Visible excitation appears to be more effective for deciphering the subtle differences in IOM maturity in response to metamorphic intensity on the different parent bodies (Quirico et al. 2018).

The stratospheric IDP L2008X3 is easily distinguished from chondrites, with its large $FWHM_G$, high I_D/I_G values, and low ω_G. This IDP also displays, for data collected at 514 nm, low $FWHM_G$ and ω_G parameters compared to primitive carbonaceous chondrites (Bonal et al., 2011). Combining 244 nm and 514 nm spectral data shows that the dispersion of the G band is $\Delta_G = (\omega_G^{244} - \omega_D^{514})/(514 - 244)$ ~ 0.015 cm^{-1}/nm slightly above dispersion values of unheated C2 chondrites (~ 0.010 cm^{-1}/nm; Quirico et al., 2014). The question arises whether these data can be interpreted in term of differences in structural order. In the case of pre-graphitic materials, the degree of structural order is assessed through the so-called Tuinstra and Koenig relationship that connect the I_D/I_G ratio with the length of coherent domains (Tuinstra and Koenig, 1970). However, this relationship does not apply to amorphous or highly disordered carbon materials, including coals and kerogens.

We follow here the framework defined by Ferrari and Robertson (2000) and Ferrari et al. (2003) that characterizes evolution stages between four end-members as graphite (G), nano-crystalline graphite (nc-G), amorphous sp^2-rich (a-C) and sp^3-rich (ta-C) carbon materials. These materials are pure or hydrogenated carbon materials formed in the laboratory. The sp^2-rich carbon materials (C-sp^3<20%) between nc-G and a-C contain a growing number of defects (bond angle and length defects) that result in shifting the position of the G-peak towards low values, increasing the G-peak dispersion and decreasing the I_D/I_G ratio. From a-C to ta-C the increase of sp^3 bonds constitutes an additional source of disorder (hybridization disorder), resulting in the decrease of I_D/I_G, and the increase of ω_G. Disorder is experimentally produced through irradiation, or formation conditions at low temperature.

386 Ordering is usually generated through annealing, which tends to increase sp^2 clustering and to
387 transform any carbon films into nc-G. For instance, the annealing of a ta-C:H film leads to the
388 sharp drop of its G-peak dispersion, the increase of I_D/I_G and the decrease of $FWHM_G$ in both
389 244 and 514 nm spectra (Ferrari and Robertson, 2001). *Thus the G-peak dispersion, $FWHM_G$*
390 *and I_D/I_G probe the degree of disorder.*

391 The low dispersion of the G-peak clearly distinguishes chondritic kerogens from
392 amorphous a-C, a-C:H and ta-C:H, and points to similarity with rather disordered nc-G. In
393 addition, the G-band peak position and its width are very similar to those of nc-G. However,
394 the use of dispersion in chondritic kerogens requires caution because they are not strictly
395 similar to carbon thin films produced in the laboratory. The abundance of sp^2 (aromatic
396 carbon) in an unheated primitive chondrite like Murchison is 60-68 % (Cody et al., 2002;
397 Gardinier et al., 2000). Around 24-28% of aliphatic carbons are detected, with ~ 20%
398 hybridized to hydrogen, which has no detectable effects on the Raman spectra (Ferrari and
399 Robertson, 2000). The remaining carbons are located in carbonyl and carboxyl groups (9-11
400 at%). Thus the presence of oxygen is a major difference with the synthetic carbon films used
401 by Ferrari and Robertson (2000) and Ferrari et al. (2003). According to results from section
402 4.1, oxygen has an effect on the Raman spectra (in fact, essentially O atoms tightly linked to
403 sp^2 clusters, e.g. ether bridge), but this effect remains weak.

404 G-peak dispersion of~ 0.015 cm^{-1}/nm for IDP L2008x3 points to an sp^2 structure very
405 close to that of nc-G. Its large $FWHM_G$ and low ω_G, in both 244 nm (this study) and 514 nm
406 data of Bonal et al. (2011) reflect a low degree of order in the decreasing ordering sequence
407 across ta-C:H, a-C:H and nc-G. In IDP W7013I1, the low signal-to-noise ratio prevents fitting
408 the 244 nm Raman spectra, but we can estimate the G-band dispersion to ~ 0.02 cm^{-1}/nm
409 using the peak position in raw data and using the 514 nm data of Bonal et al. (2011) (Table 3).
410 The higher dispersion value points to a higher degree of structural order in the IDP W7013I1

411 than in L2008x3. The 514 nm measurements of Bonal et al. (2011) also provide $FWHM_G$ and
412 ω_G values that are lower and larger than those of IDP L2008x3, respectively, also indicative
413 of higher degree of structural order.

414 Systematic measurements on stratospheric IDPs and Antarctic micro-meteorites
415 (AMMs) collected since the pioneering study of Wopenka (1988) show that (1) the G-band is
416 weakly dispersive (Starkey et al., 2013) and (2) 514 nm Raman spectra point to larger
417 $FWHM_G$ and lower ω_G parameters in comparison to primitive carbonaceous chondrites
418 (Battandier et al., 2018; Busemann et al., 2009; Dobrică et al., 2011; Merouane et al., 2013;
419 Quirico et al., 2005b). These observations, in the light of the discussion above, support the
420 view that the refractory organic materials in IDPs and AMMs have a lower degree of
421 structural order than chondritic kerogens, in the definition of Ferrari and Robertson (2000).
422
423 *4.3 Relevance of laboratory analogues*

424 The origin of chondritic organic matter is still a pending issue, and its elucidation
425 partly relies on experimental simulations that produce disordered carbonaceous materials. A
426 comprehensive study on a variety of amorphous and disordered carbonaceous materials
427 (Ferrari and Robertson, 2000) shows that polymeric a-C:H amorphous carbon displays 244
428 nm spectra fairly similar to coals, but a much larger G-peak dispersion (Ferrari and
429 Robertson, 2001). Heated ta-C:H films (600 °C) display 244 nm Raman spectra akin to those
430 of chondritic IOM and with a similar G-peak dispersion. This ta-C:H amorphous carbon was
431 formed in a radio-frequency 13.6 MHz cold plasma chamber, from a C_2H_2 gas at ~ 10^{-4} mbars
432 (Morrison et al., 1999). No insight into the CH_3/CH_2 cross-linking is provided in this
433 publication, but the infrared study of carbon films synthesized in a similar chamber from CH_4
434 shows a high CH_3/CH_2 ratio, as observed in IOM from primitive chondrites (Mutsukura and
435 Akita, 1999). This reflects a random growth of the carbon network, containing short alkyl

436 chains, at odd with the coal structure inherited from lignine and cellulose. Such materials then
437 appear as potential analogues of chondritic IOM, except they do not contain heteroatoms like
438 oxygen, nitrogen and sulfur.

439 Oxygen-bearing IOM analogues have been synthesized in the cavity of a microwave
440 (2.45 GHz) plasma reactor, for temperatures ranging between 520 and 730 °C and
441 characterized by Raman spectroscopy (Kuga et al. (2015). We have calculated their G-band
442 dispersion from their Raman spectra collected at 244 and 514 nm (Figs 3 and S2 in Kuga et
443 al., 2015) and obtained G-band dispersions in the range 0.05-0.09 cm^{-1}/nm. These values are
444 similar to those of the ta-C:H film annealed between 450 and 500 °C in Ferrari and Robertson
445 (2001), and confirm the key role of temperature in ordering carbonaceous materials.

446 Dispersion values for the synthetic materials (Kuga et al., 2015) are higher than those
447 of IOM in primitive chondrites (0.01 cm^{-1}/nm; Quirico et al. 2014). The 244 nm Raman
448 parameters of these analogues are also different from those of chondritic IOM, and of
449 immature coals (Fig. 11). These significant differences point to a different mechanism of
450 formation and evolution, suggesting that cold plasma reactions may not be a likely route of
451 formation of chondritic IOM and IDPs or that the formation process was subsequently erased
452 by metamorphism on the parent bodies of carbonaceous chondrites.

453

454 *4.4 A possible past life tracer for Early Earth and planetary exploration*

455 Complex organics are widespread across the Solar System; they have been found at
456 the surface of Mars (Freissinet et al., 2015), asteroids (Campins et al., 2010), comets
457 (Capaccioni et al., 2015), satellites of ice-giants (Cruikshank et al., 2014) and Trans-
458 Neptunian-Objects (Stern et al., 2015). The presence of organic compounds does not imply
459 the presence of life, and the identification of chemical biosignatures is a major challenge of

460 Solar System exploration (Quirico and Bonal, 2019), and in the quest of biosignatures in
461 ancient sediments on Earth.

462 Mars shows plenty of evidence for the action of liquid water, including the presence of
463 long-lasting bodies of water (i.e. the Gale crater lake, Grotzinger et al. 2014), and is a prime
464 target for the quest of bio-related organic matter. Organic matter on Mars could have different
465 endogenous or exogenous origins: *(i)* terrestrial: brought through successive space
466 missions/rovers; *(ii)* chondritic: brought by meteorites and dusts; *(iii)* synthesized through
467 biotic or abiotic processes on Mars. The high sensitivity of Raman spectroscopy to
468 carbonaceous matter has led to the presence of Raman spectrometer onboard of future landed
469 missions. The payloads of these rovers will include visible Raman (SuperCam/Mars2020-
470 NASA, RLS/ExoMars/ESA) and UV Raman (SHERLOC/ Mars2020-NASA) spectrometers
471 operating at the excitation frequency (248.6 nm) close to the one used in the present work
472 (244 nm) (Beegle et al., 2020; Wiens et al., 2016).

473

474 The 244 nm Raman spectra collected in this study efficiently discriminate chondritic
475 kerogens from immature coals and type II kerogens (Fig. 11). As far as we know, chondritic
476 OM has an abiotic origin, in contrast to terrestrial coals and kerogens derived from vascular
477 ligno-cellulosic plants, and from from algae and plankton in marine environments for type II
478 kerogens, respectively. Comparison of UV and visible Raman spectra may thus prove to be a
479 valuable tool for deciphering the biotic vs. abiotic nature of organics in old sediments both on
480 Earth and an Mars, in the event that carbonaceous materials are detected by future rovers.

481 The present study could also be useful for future *in situ* studies on the Martian surface
482 by showing the strengths and weaknesses of UV Raman to analyze organic signatures in
483 natural – and thus complex – samples. Obtaining UV spectra for raw carbonaceous chondrites
484 that typically contain 0.1 - 4 wt. % carbon (Alexander et al., 2017) is challenging. The

485 presence of major amount of silicates in these samples, which are strong UV absorbers, limits
486 the penetration depth into the samples to the very surface. Spectra of quality were obtained in
487 some studied IDPs, where the amount of organic carbon (the total carbon abundance in IDPs
488 is estimated to 15 wt. % in average; Thomas et al., 1993) is higher than in carbonaceous
489 chondrites (Alexander et al., 2017). An advantage of UV Raman is to suppress the often-
490 present and strong fluorescence background in macromolecular carbon, which may prevent
491 measurements of the Raman signal in the visible. This applies to investigations of organic
492 compound signatures, as well as to inorganic compound signatures that may be totally masked
493 by the fluorescence background. UV Raman may also be used to constrain the thermal history
494 of the carbonaceous materials. Assessing which sample has been the least modified by
495 geological processes will help in sample selections for subsequent catching and return to
496 Earth.
497
498
499
500
501 **5. CONCLUSION**
502
503 • 244 nm UV Raman spectroscopy efficiently discriminates immature abiotic
504 extraterrestrial kerogens (IOM) from terrestrial kerogens and coals, and may help in
505 recognizing potential biological origin of macromolecular carbonaceous matter
506 present in the Martian soil or in ancient rocks on Earth for a large range of degree of
507 maturity.
508 • Carbonaceous matter appears more disordered in stratospheric IDPs than in chondrites
509 from UV 244 nm Raman spectroscopy.

- The 244 nm excitation Raman spectra show that materials formed in cold plasma reactors have a different structure than chondritic organic matter, even for rather high temperature conditions (500-700 °C), suggesting that cold plasma reactions may not be a likely route for chondritic IOM formation, or that metamorphic reactions on the parent body overprinted that signature.
- The maturity of coals is rated by UV Raman spectroscopy with a structural transition observed around R_0 ~ 0.4%, which is attributed to changes in oxygen speciation.
- UV-Raman spectra of type II kerogens, even those that are highly fluorescent with a visible excitation, are easily collected. Raman spectroscopy appears here as a potential tool to provide maturity tracers of type II kerogens.

524 **ACKNOWLEDGEMENTS**

525

526 We thank three anonymous reviewers for their comments and suggestions that improved the
527 manuscript. This work has been funded by the Centre National d'Etudes Spatiales (CNES-
528 France). We thank the Museum National d'Histoire Naturelle (Paris, France) for providing the
529 meteorite samples, the Institut Français du Pétrole for the type II kerogens and the Coal
530 Sample Bank of the Penn State University for the coal samples. The Raman facility in ENS-
531 Lyon is supported by the Institut National des Sciences de l'Univers (INSU).

532

533

APPENDIX

Sample degradation is a critical issue in 244 nm Raman spectroscopy. This technique has been usually implemented on moving samples to limit the exposure to the laser beam. In the case of solid samples, a rotating sample holder with or without association to a random XY movement has been successfully used (Ferrari and Robertson, 2001; Quirico et al., 2008b). In the case of extraterrestrial material available in minute quantities, this approach is not suitable. To test the resistance of the sample to the laser beam, we first proceed with time-resolved measurements over 0-200s, during the focus optimization of the beam. Figure A1 reports tests on pure cellulose, and compare 244 nm spectra collected in this study with FT-Raman (1064 nm) (Agarwal, 2019). For a collection time of 20s, the cellulose sample starts degrading, and we observe the emergence of a broad feature at ~1600 cm^{-1}, while the rest of the spectrum still resembles that of cellulose. For a collection time of 200s, the sample is fully degraded. In the case of coals and IOMs, no dramatic evolution of the spectra is observed during the first tens of seconds. As these materials have experienced thermal processing in their natural host rocks, we think that the effect of an ultra-fast (< 5s) processing under the laser beam is unlikely.

Another issue is that of the evolution of the Raman spectra over a longer time, due to oxidation processes (Quirico et al., 2005a). Figure A2 reports the Raman spectra collected continuously for a collection time of 150s for each spectrum, under air and in a cell under an argon atmosphere. The results are qualitatively similar with those obtained with a 514 nm excitation: a progressive drop of the intensity, and slight spectral changes that lead to changes of the Raman parameters (Fig. A3). The Ar environment only slightly improves the data, and we observe that the evolution trend of the Raman parameters is much smaller than the

558 dispersion due to sample heterogeneity or other factors not clearly identified (e.g. sample
559 topography, porosity, etc.).
560

RESEARCH DATA

Research Data associated with this article can be accessed from through the SSHADE/GHOST database (https://www.sshade.eu/), at https://doi.org/10.26302/SSHADE/EXPERIMENT_LB_20200414_001

REFERENCES

Agarwal, U.P. (2019). Analysis of Cellulose and Lignocellulose Materials by Raman Spectroscopy: A Review of the Current Status. Molecules *24*, 1659.

Alexander, C.M.O., Cody, G.D., De Gregorio, B.T., Nittler, L.R., and Stroud, R.M. (2017). The nature, origin and modification of insoluble organic matter in chondrites, the major source of Earth's C and N. Chem. Erde - Geochem. *77*, 227–256.

Asher (1993). UV Raman Spectroscopy for Analytical, Physical, and Biophysical chemistry. *65*, 59–66.

Battandier, M., Bonal, L., Quirico, E., Beck, P., Engrand, C., Duprat, J., and Dartois, E. (2018). Characterization of the organic matter and hydration state of Antarctic micrometeorites: A reservoir distinct from carbonaceous chondrites. Icarus *306*, 74–93.

Beegle, L.W., Bhartia, R., DeFlores, L., Abbey, W., Miller, E., Bailey, Z., Razzell Hollis, J., Pollack, R., Asher, S., Burton, A., et al. (2020). The SHERLOC Investigation on the Mars 2020 Rover. In Lunar and Planetary Science Conference, p. 2081.

Beyssac, O., Goffé, B., Chopin, C., and Rouzaud, J.N. (2002). Raman spectra of carbonaceous material in metasediments: a new geothermometer: RAMAN SPECTROSCOPY OF CARBONACEOUS MATERIAL. J. Metamorph. Geol. *20*, 859–871.

Bonal, L., Quirico, E., Bourot-Denise, M., and Montagnac, G. (2006). Determination of the petrologic type of CV3 chondrites by Raman spectroscopy of included organic matter. Geochim. Cosmochim. Acta *70*, 1849–1863.

Bonal, L., Bourot-Denise, M., Quirico, E., Montagnac, G., and Lewin, E. (2007). Organic matter and metamorphic history of CO chondrites. Geochim. Cosmochim. Acta *71*, 1605–1623.

Bonal, L., Quirico, E., and Montagnac, G. (2011). Structure of Primitive Polyaromatic Carbonaceous Matter: IDPs vs. Chondrites. Meteorit. Planet. Sci. Suppl. *74*, 5125.

Bonal, L., Quirico, E., Flandinet, L., and Montagnac, G. (2016). Thermal history of type 3 chondrites from the Antarctic meteorite collection determined by Raman spectroscopy of their polyaromatic carbonaceous matter. Geochim. Cosmochim. Acta *189*, 312–337.

Bonnet, J.-Y., Quirico, E., Buch, A., Thissen, R., Szopa, C., Carrasco, N., Cernogora, G., Fray, N., Cottin, H., Roy, L.L., et al. (2015). Formation of analogs of cometary nitrogen-rich refractory organics from thermal degradation of tholin and HCN polymer. Icarus *250*, 53–63.

Bower, D.M., Steele, A., Fries, M.D., and Kater, L. (2013). Micro Raman Spectroscopy of Carbonaceous Material in Microfossils and Meteorites: Improving a Method for Life Detection. Astrobiology *13*, 103–113.

Busemann, H., Nguyen, A.N., Cody, G.D., Hoppe, P., Kilcoyne, A.L.D., Stroud, R.M., Zega, T.J., and Nittler, L.R. (2009). Ultra-primitive interplanetary dust particles from the comet 26P/Grigg–Skjellerup dust stream collection. Earth Planet. Sci. Lett. *288*, 44–57.

Campins, H., Hargrove, K., Pinilla-Alonso, N., Howell, E.S., Kelley, M.S., Licandro, J., Mothé-Diniz, T., Fernández, Y., and Ziffer, J. (2010). Water ice and organics on the surface of the asteroid 24 Themis. Nature *464*, 1320–1321.

Capaccioni, F., Coradini, A., Filacchione, G., Erard, S., Arnold, G., Drossart, P., De Sanctis, M.C., Bockelee-Morvan, D., Capria, M.T., Tosi, F., et al. (2015). The organic-rich surface of comet 67P/Churyumov-Gerasimenko as seen by VIRTIS/Rosetta. Science *347*, aaa0628–aaa0628.

Chen, Y., Mastalerz, M., and Schimmelmann, A. (2012). Characterization of chemical functional groups in macerals across different coal ranks via micro-FTIR spectroscopy. Int. J.

618 Coal Geol. *104*, 22–33.
619 Cody, G.D., and Alexander, C.M.O. 'D. (2005). NMR studies of chemical structural
620 variation of insoluble organic matter from different carbonaceous chondrite groups. Geochim.
621 Cosmochim. Acta *69*, 1085–1097.
622 Cody, G.D., Alexander, C.M.O., and Tera, F. (2002). Solid-state (1 H and 13 C)
623 nuclear magnetic resonance spectroscopy of insoluble organic residue in the Murchison
624 meteorite: a self-consistent quantitative analysis. Geochim. Cosmochim. Acta *66*, 1851–1865.
625 Cruikshank, D.P., Dalle Ore, C.M., Clark, R.N., and Pendleton, Y.J. (2014). Aromatic
626 and aliphatic organic materials on Iapetus: Analysis of Cassini VIMS data. Icarus *233*, 306–
627 315.
628 Dartois, E., Engrand, C., Brunetto, R., Duprat, J., Pino, T., Quirico, E., Remusat, L.,
629 Bardin, N., Briani, G., Mostefaoui, S., et al. (2013). UltraCarbonaceous Antarctic
630 micrometeorites, probing the Solar System beyond the nitrogen snow-line. Icarus *224*, 243–
631 252.
632 Dobrică, E., Engrand, C., Quirico, E., Montagnac, G., and Duprat, J. (2011). Raman
633 characterization of carbonaceous matter in CONCORDIA Antarctic micrometeorites: Raman
634 characterization of carbonaceous matter in micrometeorites. Meteorit. Planet. Sci. *46*, 1363–
635 1375.
636 Ferrari, A.C., and Robertson, J. (2000). Interpretation of Raman spectra of disordered
637 and amorphous carbon. Phys. Rev. B *61*, 14095–14107.
638 Ferrari, A.C., and Robertson, J. (2001). Resonant Raman spectroscopy of disordered,
639 amorphous, and diamondlike carbon. Phys. Rev. B *64*, 075414.
640 Ferrari, A.C., Rodil, S.E., and Robertson, J. (2003). Interpretation of infrared and
641 Raman spectra of amorphous carbon nitrides. Phys. Rev. B *67*, 155306.
642 Foucher, F. (2019). Detection of Biosignatures Using Raman Spectroscopy. In
643 Biosignatures for Astrobiology, B. Cavalazzi, and F. Westall, eds. (Cham: Springer
644 International Publishing), pp. 267–282.
645 Freissinet, C., Glavin, D.P., Mahaffy, P.R., Miller, K.E., Eigenbrode, J.L., Summons,
646 R.E., Brunner, A.E., Buch, A., Szopa, C., Archer, P.D., et al. (2015). Organic molecules in the
647 Sheepbed Mudstone, Gale Crater, Mars: Detection of organics in martian sample. J. Geophys.
648 Res. Planets *120*, 495–514.
649 Gardinier, A., Derenne, S., Robert, F., Behar, F., Largeau, C., and Maquet, J. (2000).
650 Solid state CP/MAS 13 C NMR of the insoluble organic matter of the Orgueil and Murchison
651 meteorites: quantitative study. Earth Planet. Sci. Lett. *184*, 9–21.
652 Grotzinger, J.P., Sumner, D.Y., Kah, L.C., Stack, K., Gupta, S., Edgar, L., Rubin, D.,
653 Lewis, K., Schieber, J., Mangold, N., et al. (2014). A Habitable Fluvio-Lacustrine
654 Environment at Yellowknife Bay, Gale Crater, Mars. Science *343*, 1242777–1242777.
655 Jehlička, J., and Edwards, H.G.M. (2008). Raman spectroscopy as a tool for the non-
656 destructive identification of organic minerals in the geological record. Org. Geochem. *39*,
657 371–386.
658 Jehlička, J., Urban, O., and Pokorný, J. (2003). Raman spectroscopy of carbon and solid
659 bitumens in sedimentary and metamorphic rocks. Spectrochim. Acta. A. Mol. Biomol.
660 Spectrosc. *59*, 2341–2352.
661 Kelemen, S.R., and Fang, H.L. (2001). Maturity Trends in Raman Spectra from
662 Kerogen and Coal. Energy Fuels *15*, 653–658.
663 Kouketsu, Y., Mizukami, T., Mori, H., Endo, S., Aoya, M., Hara, H., Nakamura, D.,
664 and Wallis, S. (2014). A new approach to develop the Raman carbonaceous material
665 geothermometer for low-grade metamorphism using peak width: Raman CM geothermometer
666 using FWHM. Isl. Arc *23*, 33–50.
667 Kuga, M., Marty, B., Marrocchi, Y., and Tissandier, L. (2015). Synthesis of refractory

668 organic matter in the ionized gas phase of the solar nebula. Proc. Natl. Acad. Sci. *112*, 7129–
669 7134.
670 Lahfid, A., Beyssac, O., Deville, E., Negro, F., Chopin, C., and Goffé, B. (2010).
671 Evolution of the Raman spectrum of carbonaceous material in low-grade metasediments of
672 the Glarus Alps (Switzerland): RSCM in low-grade metasediments. Terra Nova *22*, 354–360.
673 Merlen, A., Buijnsters, J., and Pardanaud, C. (2017). A Guide to and Review of the Use
674 of Multiwavelength Raman Spectroscopy for Characterizing Defective Aromatic Carbon
675 Solids: from Graphene to Amorphous Carbons. Coatings *7*, 153.
676 Merouane, S., Djouadi, Z., and Le Sergeant d'Hendecourt, L. (2013). Relations between
677 aliphatics and silicate components inn 12 stratospheric particles deduced from virational
678 spectroscopy. Astrophys. J. *780*, 174.
679 Morrison, N.A., Rodil, S.E., Ferrari, A.C., Robertson, J., and Milne, W.I. (1999). High
680 rate deposition of ta-C:H using an electron cyclotron wave resonance plasma source. Thin
681 Solid Films 3.
682 Mutsukura, N., and Akita, K. (1999). Infrared absorption spectroscopy measurements of
683 amorphous CNx ®lms prepared in CH4/N2 r.f. discharge. Thin Solid Films 5.
684 Petersen, H.I., Rosenberg, P., and Nytoft, H.P. (2008). Oxygen groups in coals and
685 alginite-rich kerogen revisited. Int. J. Coal Geol. *74*, 93–113.
686 Potgieter-Vermaak, S., Maledi, N., Wagner, N., Van Heerden, J.H.P., Van Grieken, R.,
687 and Potgieter, J.H. (2011). Raman spectroscopy for the analysis of coal: a review. J. Raman
688 Spectrosc. *42*, 123–129.
689 Quirico, E., and Bonal, L. (2019). Organic Matter in Interplanetary Dusts and
690 Meteorites. In Biosignatures for Astrobiology, Advances in Astrobiology and Biogeophysics.
691 ISBN 978-3-319-96174-3. Springer Nature Switzerland AG, 2019, p. 23, p. 23.
692 Quirico, E., Raynal, P.-I., and Bourot-denise, M. (2003). Metamorphic grade of organic
693 matter in six unequilibrated ordinary chondrites. Met. Plan. Sci. *38*, 795–811.
694 Quirico, E., Rouzaud, J.-N., Bonal, L., and Montagnac, G. (2005a). Maturation grade of
695 coals as revealed by Raman spectroscopy: Progress and problems. Spectrochim. Acta. A.
696 Mol. Biomol. Spectrosc. *61*, 2368–2377.
697 Quirico, E., Borg, J., Raynal, P.-I., Montagnac, G., and d'Hendecourt, L. (2005b). A
698 micro-Raman survey of 10 IDPs and 6 carbonaceous chondrites. Planet. Space Sci. *53*, 1443–
699 1448.
700 Quirico, E., Szopa, C., Cernogora, G., Lees, V., Derenne, S., McMillan, P.F.,
701 Montagnac, G., Reynard, B., Rouzaud, J.-N., Fray, N., et al. (2008). Tholins and their
702 relevance for astrophysical issues. Proc. Int. Astron. Union *4*, 409–416.
703 Quirico, E., Montagnac, G., Rouzaud, J.-N., Bonal, L., Bourot-Denise, M., Duber, S.,
704 and Reynard, B. (2009). Precursor and metamorphic condition effects on Raman spectra of
705 poorly ordered carbonaceous matter in chondrites and coals. Earth Planet. Sci. Lett. *287*, 185–
706 193.
707 Quirico, E., Orthous-Daunay, F.-R., Beck, P., Bonal, L., Brunetto, R., Dartois, E., Pino,
708 T., Montagnac, G., Rouzaud, J.-N., Engrand, C., et al. (2014). Origin of insoluble organic
709 matter in type 1 and 2 chondrites: New clues, new questions. Geochim. Cosmochim. Acta
710 *136*, 80–99.
711 Quirico, E., Bonal, L., Beck, P., Alexander, C.M.O., Yabuta, H., Nakamura, T., Nakato,
712 A., Flandinet, L., Montagnac, G., Schmitt-Kopplin, P., et al. (2018). Prevalence and nature of
713 heating processes in CM and C2-ungrouped chondrites as revealed by insoluble organic
714 matter. Geochim. Cosmochim. Acta *241*, 17–37.
715 Remusat, L., Derenne, S., and Robert, F. (2005a). New insight on aliphatic linkages in
716 the macromolecular organic fraction of Orgueil and Murchison meteorites through ruthenium
717 tetroxide oxidation. Geochim. Cosmochim. Acta *69*, 4377–4386.

Remusat, L., Derenne, S., Robert, F., and Knicker, H. (2005b). New pyrolytic and spectroscopic data on Orgueil and Murchison insoluble organic matter: A different origin than soluble? Geochim. Cosmochim. Acta *69*, 3919–3932.

Ribeiro-Soares, J., Cançado, L.G., Falcão, N.P.S., Martins Ferreira, E.H., Achete, C.A., and Jorio, A. (2013). The use of Raman spectroscopy to characterize the carbon materials found in Amazonian anthrosoils: Raman spectroscopy for carbon materials in Amazonian anthrosoils. J. Raman Spectrosc. *44*, 283–289.

Sforna, M.C., van Zuilen, M.A., and Philippot, P. (2014). Structural characterization by Raman hyperspectral mapping of organic carbon in the 3.46 billion-year-old Apex chert, Western Australia. Geochim. Cosmochim. Acta *124*, 18–33.

Shkolyar, S., Eshelman, E.J., Farmer, J.D., Hamilton, D., Daly, M.G., and Youngbull, C. (2018). Detecting Kerogen as a Biosignature Using Colocated UV Time-Gated Raman and Fluorescence Spectroscopy. Astrobiology *18*, 431–453.

Smudde, G.H., Slager, T.L., and Coe, C.G. (1995). DRIFTS and Raman Investigation of N2 and 02 Adsorption on Zeolites at Ambient Temperature. Appli. Spec. *49*, 1747–1755.

Starkey, N.A., Franchi, I.A., and Alexander, C.M.O. (2013). A Raman spectroscopic study of organic matter in interplanetary dust particles and meteorites using multiple wavelength laser excitation. Meteorit. Planet. Sci. *48*, 1800–1822.

Steele, A., McCubbin, F.M., and Fries, M.D. (2016). The provenance, formation, and implications of reduced carbon phases in Martian meteorites. Meteorit. Planet. Sci. *51*, 2203–2225.

Steele, A., Benning, L.G., Wirth, R., Siljeström, S., Fries, M.D., Hauri, E., Conrad, P.G., Rogers, K., Eigenbrode, J., Schreiber, A., et al. (2018). Organic synthesis on Mars by electrochemical reduction of CO_2. Sci. Adv. *4*, eaat5118.

Stern, S.A., Bagenal, F., Ennico, K., Gladstone, G.R., Grundy, W.M., McKinnon, W.B., Moore, J.M., Olkin, C.B., Spencer, J.R., Weaver, H.A., et al. (2015). The Pluto system: Initial results from its exploration by New Horizons. Science *350*, aad1815–aad1815.

Thomas, K.L., Blandford, G.E., Keller, L.P., and Klock, W. (1993). Thomas93_GCA_57_1551.pdf. David S *57*, 1551–1566.

Tuinstra, F., and Koenig, L. (1970). Raman Spectrum of Graphite. J. Chem. Phys. *53*, 1126–1130.

Van Krevelen, D.W. (1993). Coal: typology - physics - chemistry - constitution (Elsevier Science Publishers, Amsterdam (Netherlands)).

Vandenbroucke, M., and Largeau, C. (2007). Kerogen origin, evolution and structure. Org. Geochem. *38*, 719–833.

Wang, Y., Huang, Y., Alexander, C.M.O. 'D., Fogel, M., and Cody, G. (2005). Molecular and compound-specific hydrogen isotope analyses of insoluble organic matter from different carbonaceous chondrite groups. Geochim. Cosmochim. Acta *69*, 3711–3721.

Wiens, R.C., Maurice, S., McCabe, K., Cais, P., Anderson, R.B., Beyssac, O., Bonal, L., Clegg, S., Deflores, L., Fischer, W.W., et al. (2016). THE SUPERCAM REMOTE SENSING INSTRUMENT SUITE FOR MARS 2020. (Houston, USA), p. 2.

Wopenka, B. (1988). Raman observations on individual interplanetary dust particles. Earth Planet. Sci. Lett. *88*, 221–231.

762

763 **FIGURES CAPTIONS**

764

765 **Figure 1:** The experimental set up used to enrich matrix grains in carbonaceous matter by
766 applying a HF/HCl acid treatment. (a) The alumina chamber purged with Ar, binocular
767 microscope and a peristaltic pump providing and extracting reagents and distilled water for
768 neutralization. (b) A Teflon sample holder contain a gold foil onto which matrix grains are
769 deposed. Inlet for injection and extraction of liquids are handled by two micromanipulator. (c)
770 Scanning Electron Microscopy image of matrix grains after the HF/HCl treatment.

771

772 **Figure 2:** The Lorentzian-Breit-Wigner-Fano spectral decomposition of the first-order carbon
773 bands.

774

775 **Figure 3:** Raman spectra of the immature coal PSOC 1532 (left) and of polyaromatic matter
776 of the Murchison chondrite (right). Top: normalized baseline-corrected spectra. Bottom: raw
777 spectra. Note the low fluorescence and the lower D-band intensity in 244 nm spectra.

778

779 **Figure 4:** Raman spectra of mature coals (Ro > 1%, indicated for each spectrum).

780

781 **Figure 5:** (a): Raman spectra of immature coals (Ro < 1%) (top); (b) type II kerogens; (c):.
782 same spectra vertically shifted to enhance clarity.

783

784 **Figure 6:** The Raman spectral parameters of mature coals (Ro > 1%) plotted against the mean
785 maximum vitrinite reflectance. The dotted blue lines are a guide to the eyes.

786

Figure 7: The Raman spectral parameters of immature coals (Ro < 1%) plotted against the mean maximum vitrinite reflectance. The dotted blue lines are a guide to the eyes.

Figure 8: $FWHM_D$ vs. I_D/I_G and $FWHM_G$ vs. ω_D diagrams, for type II kerogens and immature coals (Ro < 1%).

Figure 9: 244 nm Raman spectra of Murchison as: raw matrix grains, Insoluble Organic Matter, and matrix grains treated with the micro-extraction device (see text).

Figure 10: 244 nm Raman spectra of primitive carbonaceous chondrites and IDP L2008x3.

Figure 11: $FWHM_D$ vs. I_D/I_G (a), $FWHM_G$ vs. ω_G (b) and A_{DDG} vs. ω_D (c) diagrams corresponding to coals, type II kerogen, chondritic IOM, IDP L2008x3 and analogs of Kuga et al. (2015). (d): comparison of corresponding Raman spectra, which clearly distinguishes sedimentary organic matter, chondritic IOM and IDP. Note that the data from Kuga et al. (2015) have been rescaled due to the use of different fit models.

Figure 12: Raman spectra of stratospheric IDPs L2008x3 and W7013I1. The blow up shows the 1900-2500 cm^{-1} spectral range for two individual spectra (red) and smoothed spectra (blue). The weak features at 2220 and 2320 cm^{-1} are assigned to the cyanide group –CN and adsorbed N_2, respectively.

Figure 13: The $FWHM_G$ versus ω_G diagram of 514 nm Raman data earlier published in Quirico et al. (2003). This diagram clearly distinguishes coals with Ro < 0.4% and 0.4 < Ro < 1%, in agreement with spectra collected with a 244 nm excitation (Fig. 7).

Figure A1: The spectrum of cellulose collected at 244 nm during 20 and 200 s, compared to the FT-Raman (1064 nm) of amorphous cellulose (Agarwal, 2019).

Figure A2: Automatic collection of 244 nm Raman spectra (acquisition duration 150 s; grating 600 gr/mm).

Figure A3: The Raman parameters derived from the spectra shown in figure A2, with a LBWF fit. The error bars are the standard deviation calculated from the data collected at different locations of the Murchison IOM, under air and with a collection time of 2x150s (Tab. 2).

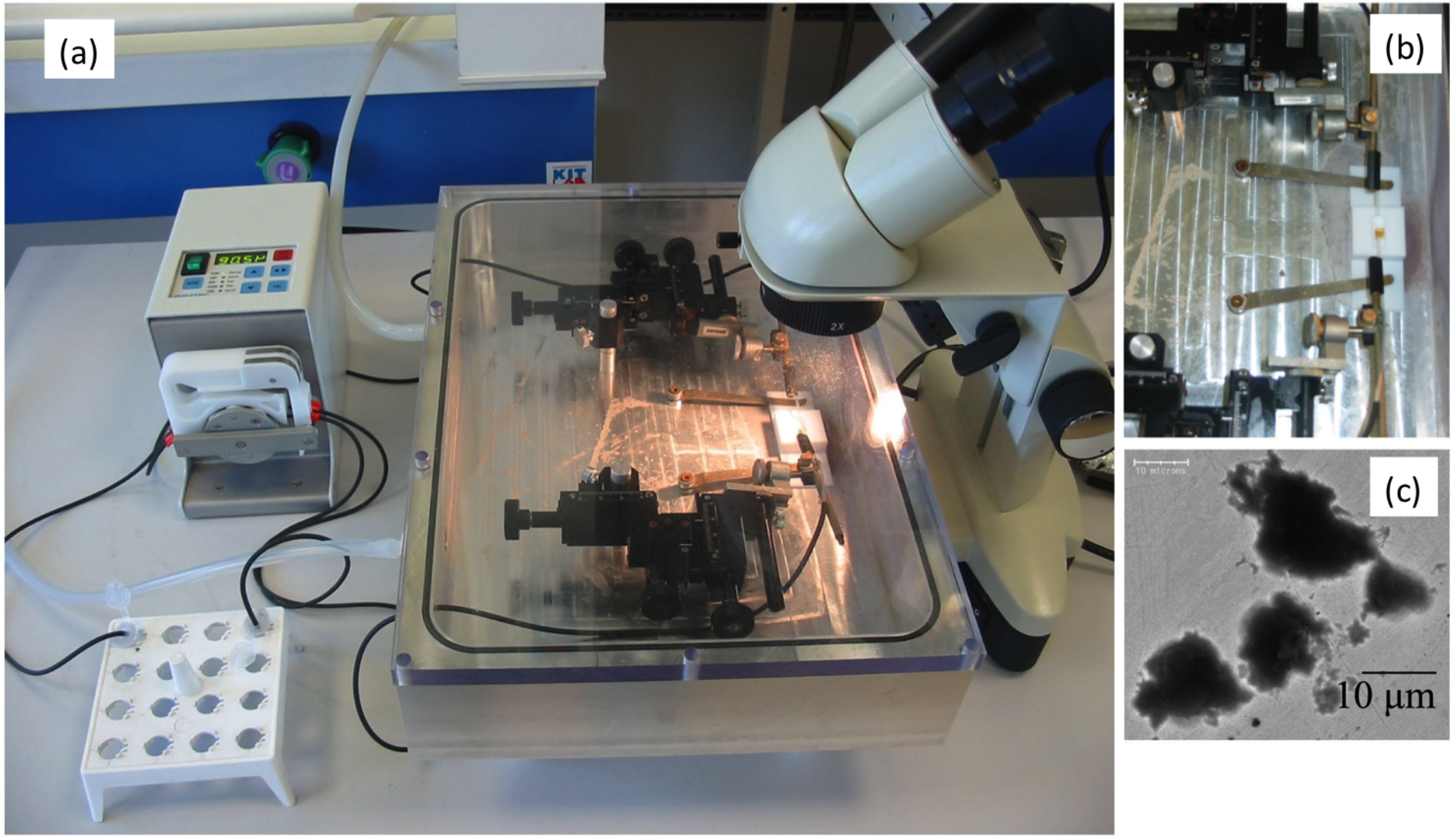
(a)
(b)
(c)
10 µm

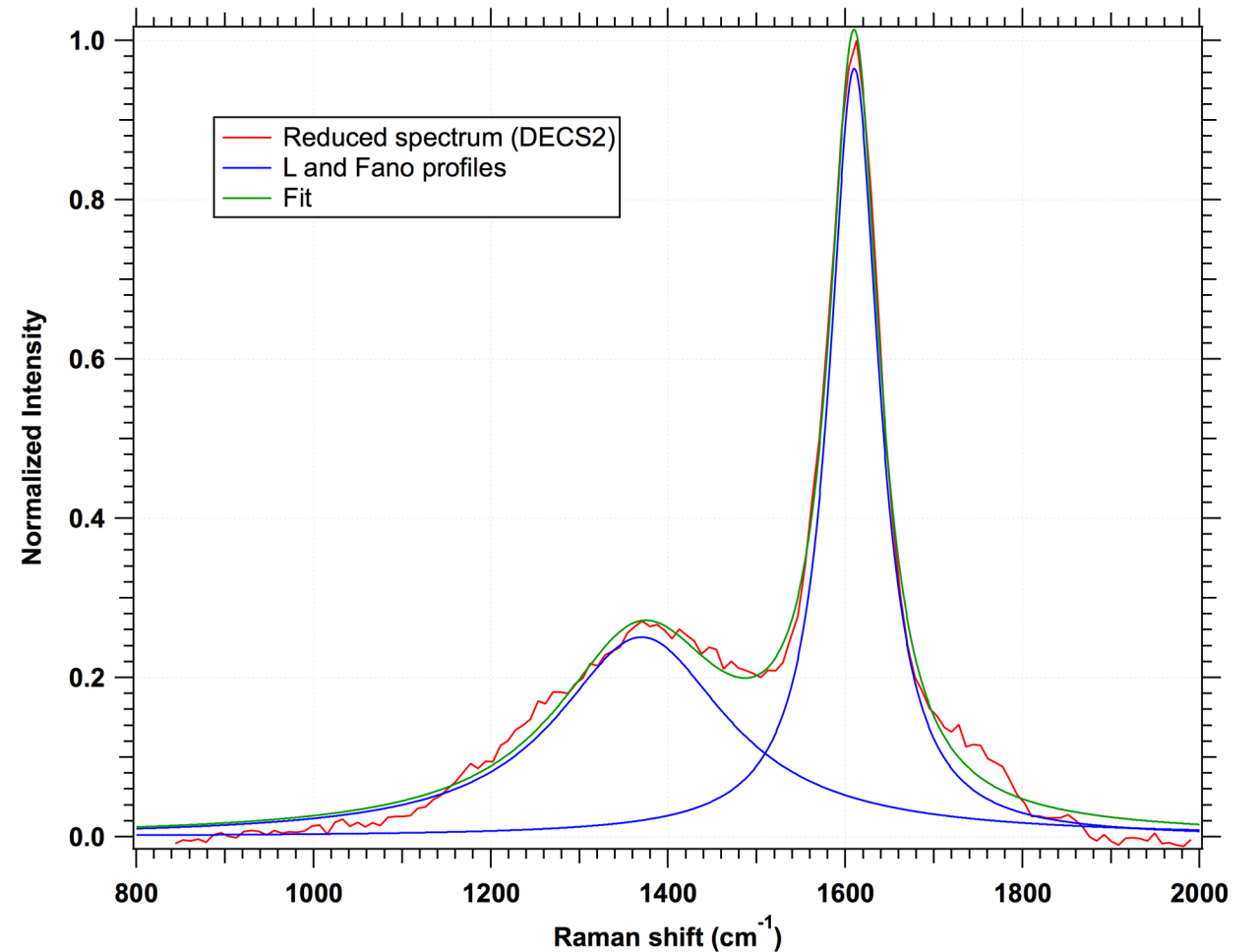
Reduced spectrum (DECS2)
L and Fano profiles
Fit
Normalized Intensity
1.0
0.8
0.6
0.4
0.2
0.0
800
1000
1200
1400
1600
1800
2000
Raman shift (cm-1)

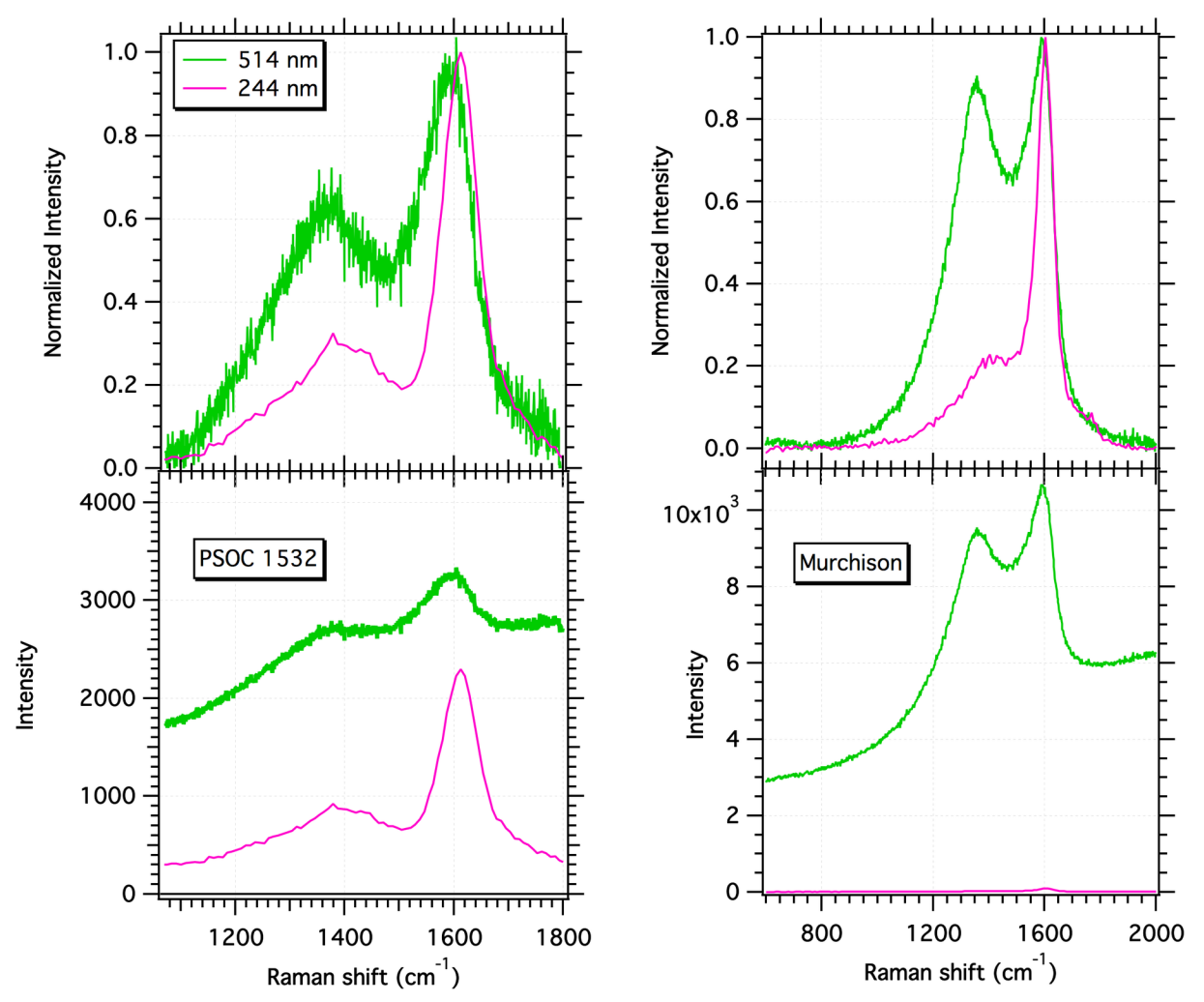
514 nm
244 nm
Normalized Intensity
PSOC 1532
Intensity
Raman shift (cm-1)
Murchison
10x10^3
Intensity
Raman shift (cm-1)

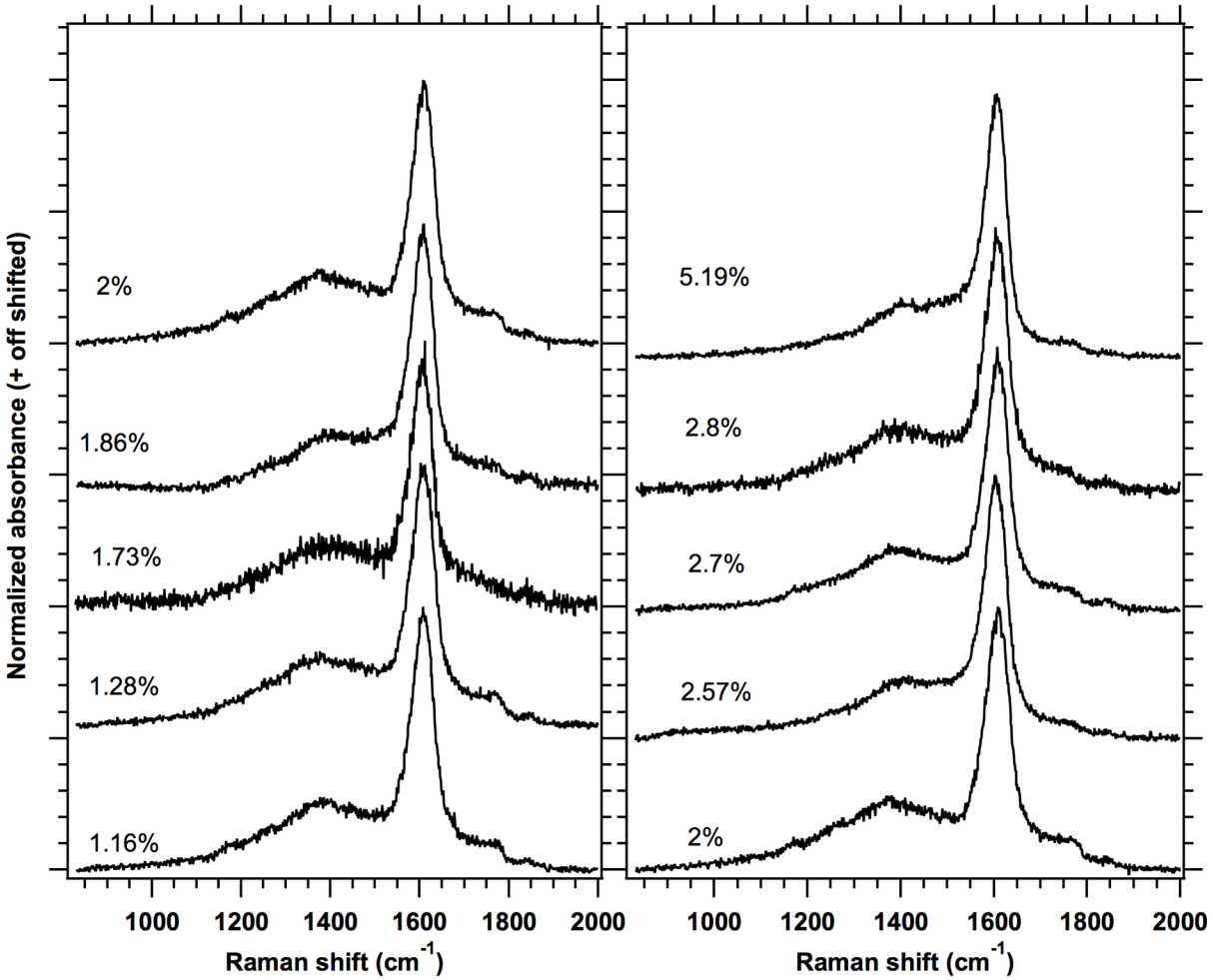
Normalized absorbance (+ off shifted)
2%
1.86%
1.73%
1.28%
1.16%
5.19%
2.8%
2.7%
2.57%
2%
1000
1200
1400
1600
1800
2000
Raman shift (cm-1)
Raman shift (cm-1)

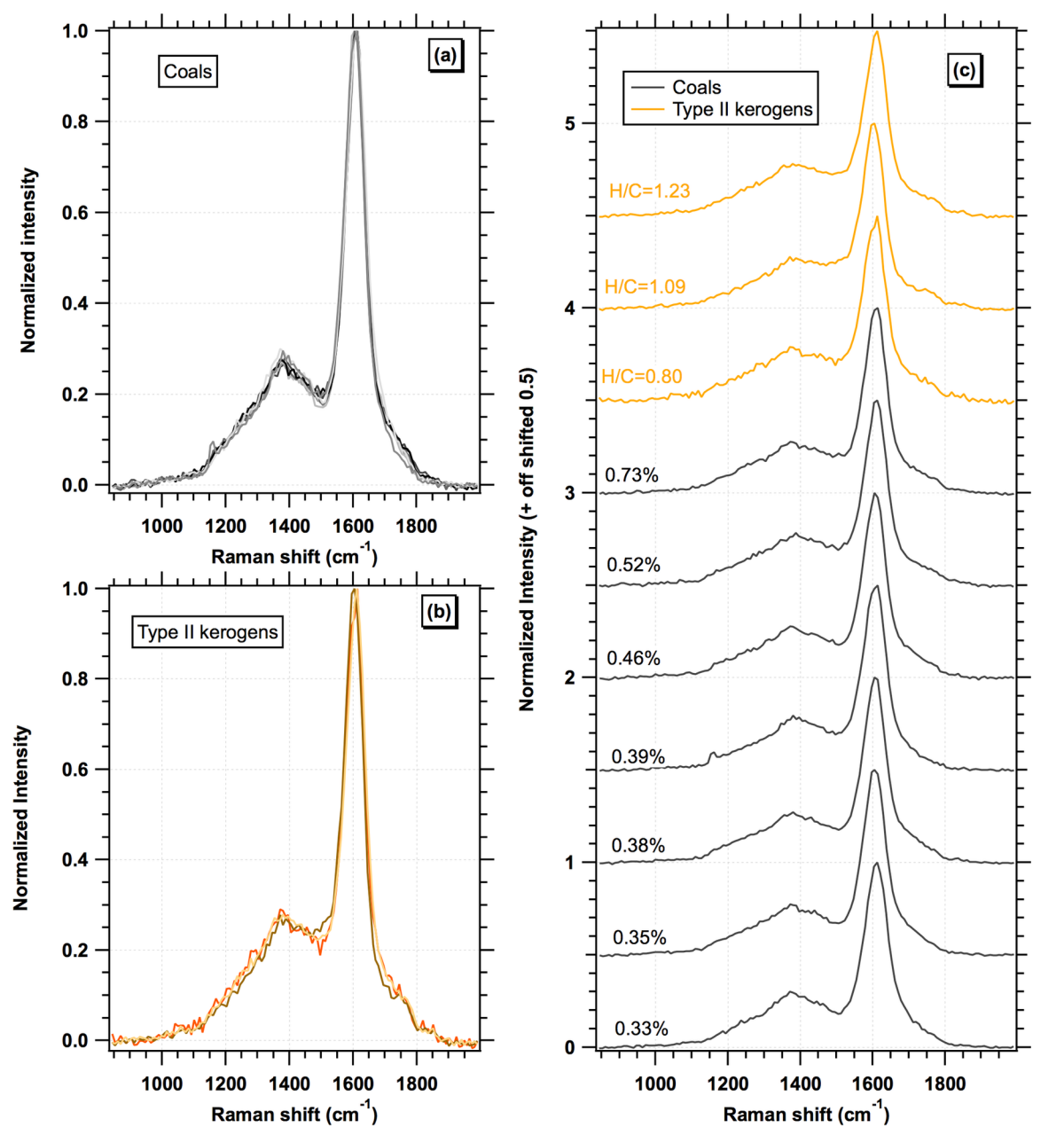
Coals
(a)
Normalized intensity
Raman shift (cm-1)
Type II kerogens
(b)
Normalized Intensity
Raman shift (cm-1)
Coals
Type II kerogens
(c)
H/C=1.23
H/C=1.09
H/C=0.80
0.73%
0.52%
0.46%
0.39%
0.38%
0.35%
0.33%
Normalized Intensity (+ off shifted 0.5)
Raman shift (cm-1)

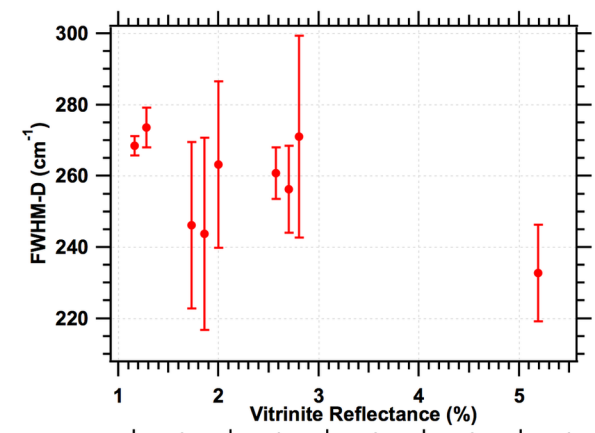
FWHM-D (cm-1)
Vitrinite Reflectance (%)

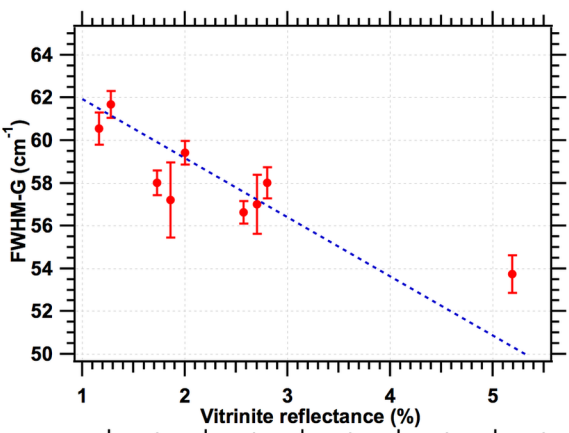
FWHM-G (cm-1)
Vitrinite reflectance (%)

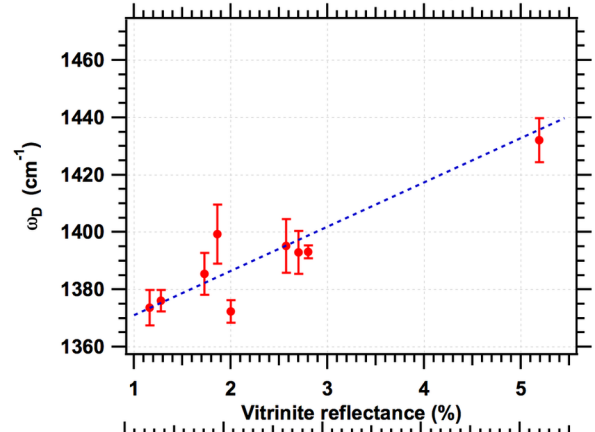
ωD (cm-1)
Vitrinite reflectance (%)

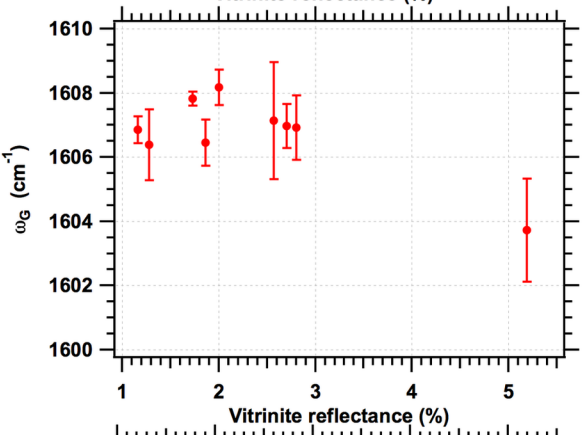
ωG (cm-1)
Vitrinite reflectance (%)

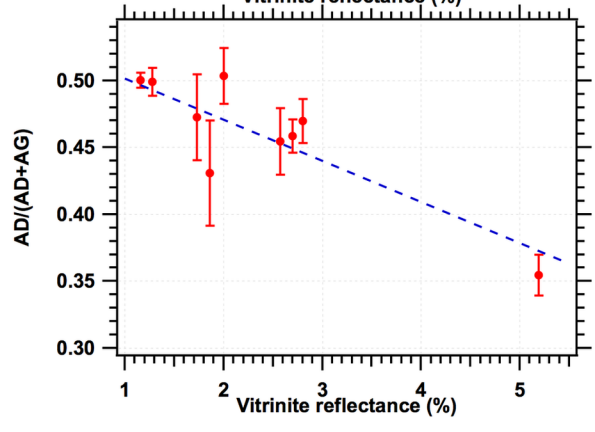
AD/(AD+AG)
Vitrinite reflectance (%)

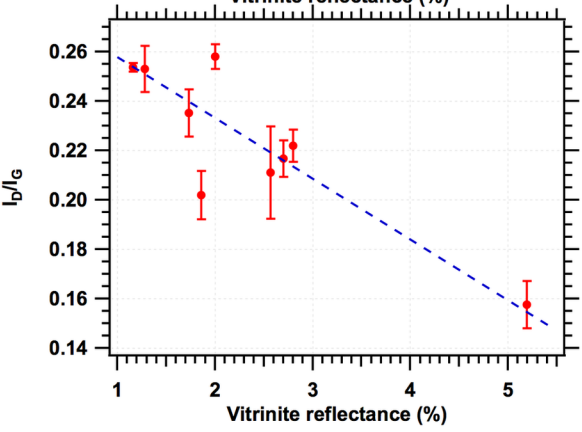
ID/IG
Vitrinite reflectance (%)

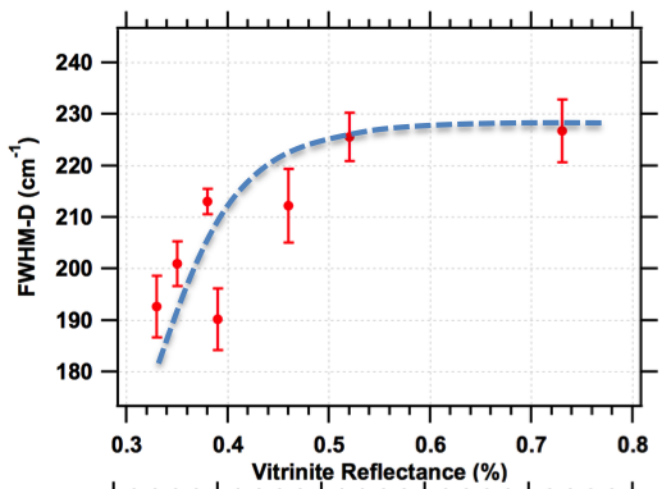
FWHM-D (cm-1)
240
230
220
210
200
190
180
0.3
0.4
0.5
0.6
0.7
0.8
Vitrinite Reflectance (%)

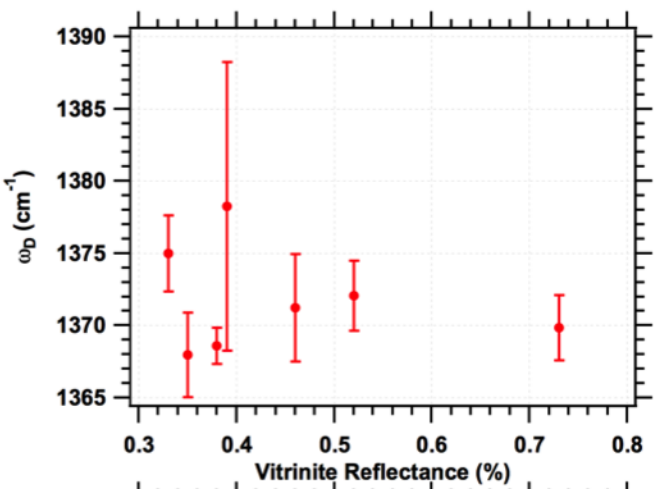
ωD (cm-1)
1390
1385
1380
1375
1370
1365
0.3
0.4
0.5
0.6
0.7
0.8
Vitrinite Reflectance (%)

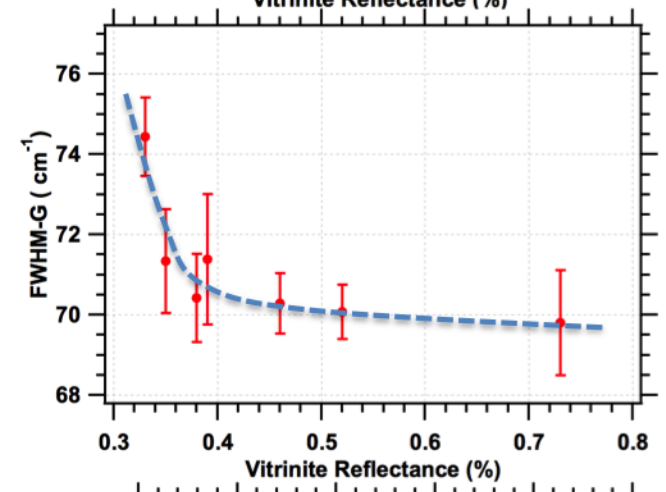
FWHM-G (cm-1)
76
74
72
70
68
0.3
0.4
0.5
0.6
0.7
0.8
Vitrinite Reflectance (%)

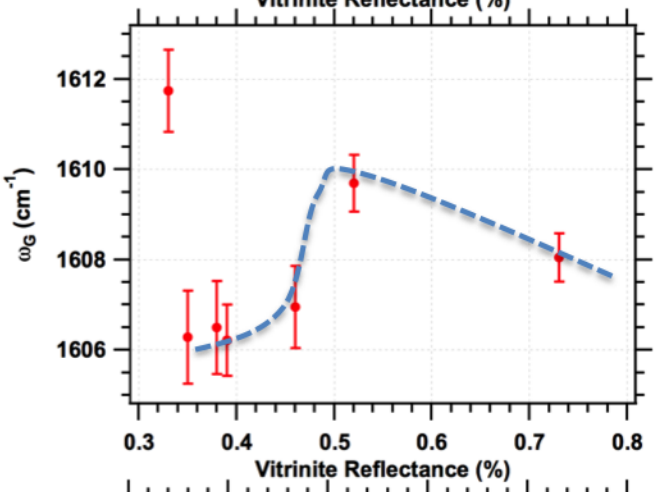
ωG (cm-1)
1612
1610
1608
1606
0.3
0.4
0.5
0.6
0.7
0.8
Vitrinite Reflectance (%)

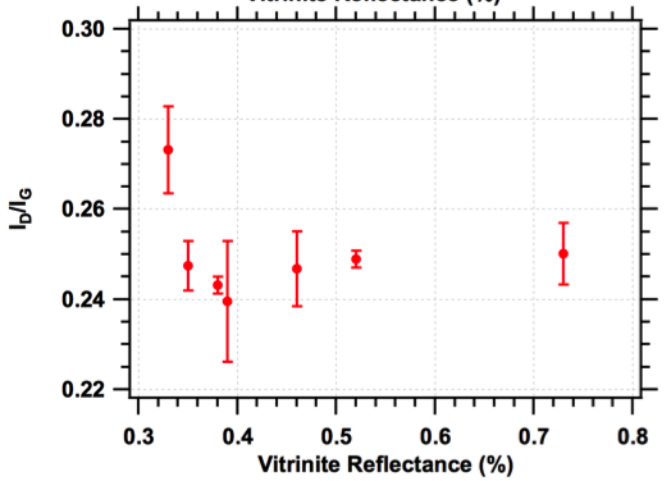
ID/IG
0.30
0.28
0.26
0.24
0.22
0.3
0.4
0.5
0.6
0.7
0.8
Vitrinite Reflectance (%)

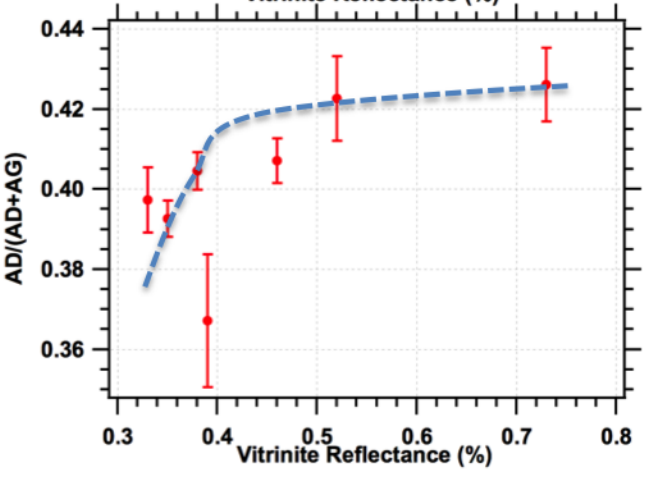
AD/(AD+AG)
0.44
0.42
0.40
0.38
0.36
0.3
0.4
0.5
0.6
0.7
0.8
Vitrinite Reflectance (%)

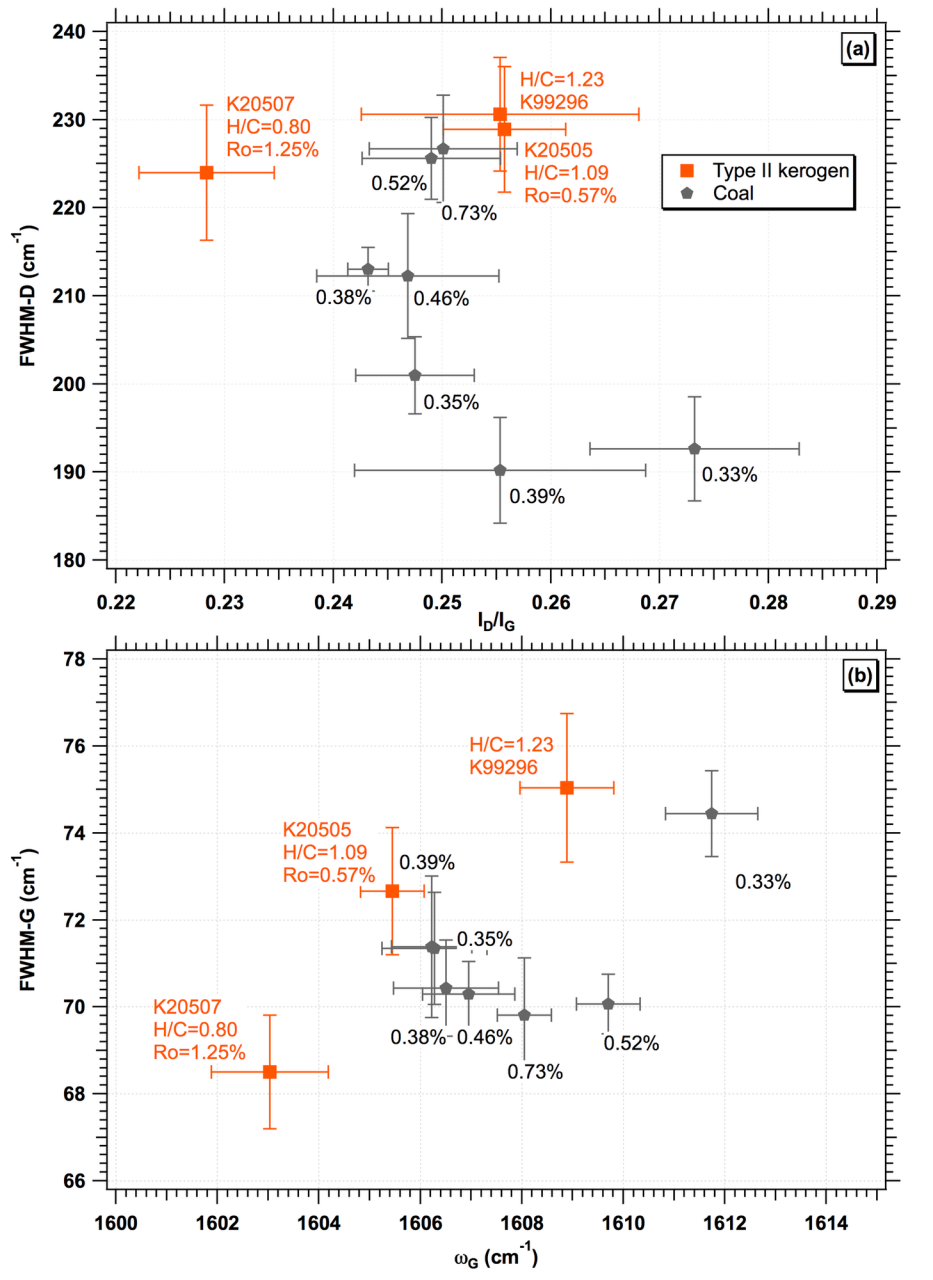
(a)
FWHM-D (cm-1)
ID/IG
K20507
H/C=0.80
Ro=1.25%
H/C=1.23
K99296
K20505
H/C=1.09
Ro=0.57%
Type II kerogen
Coal
0.52%
0.73%
0.38%
0.46%
0.35%
0.33%
0.39%
(b)
FWHM-G (cm-1)
ωG (cm-1)
H/C=1.23
K99296
K20505
H/C=1.09
Ro=0.57%
0.39%
0.33%
0.35%
K20507
H/C=0.80
Ro=1.25%
0.38%
0.46%
0.52%
0.73%

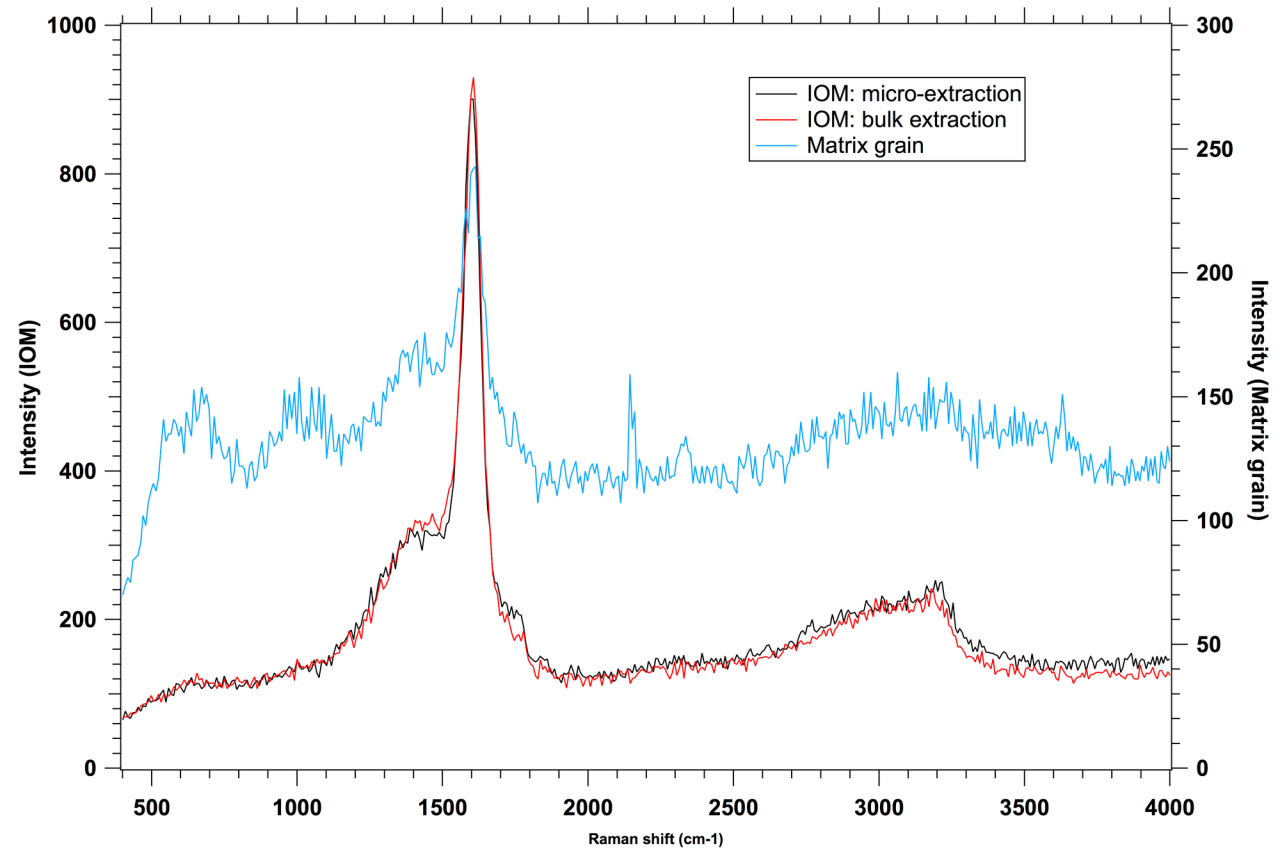
IOM: micro-extraction
IOM: bulk extraction
Matrix grain
Intensity (IOM)
Intensity (Matrix grain)
Raman shift (cm-1)
0
200
400
600
800
1000
0
50
100
150
200
250
300
500
1000
1500
2000
2500
3000
3500
4000

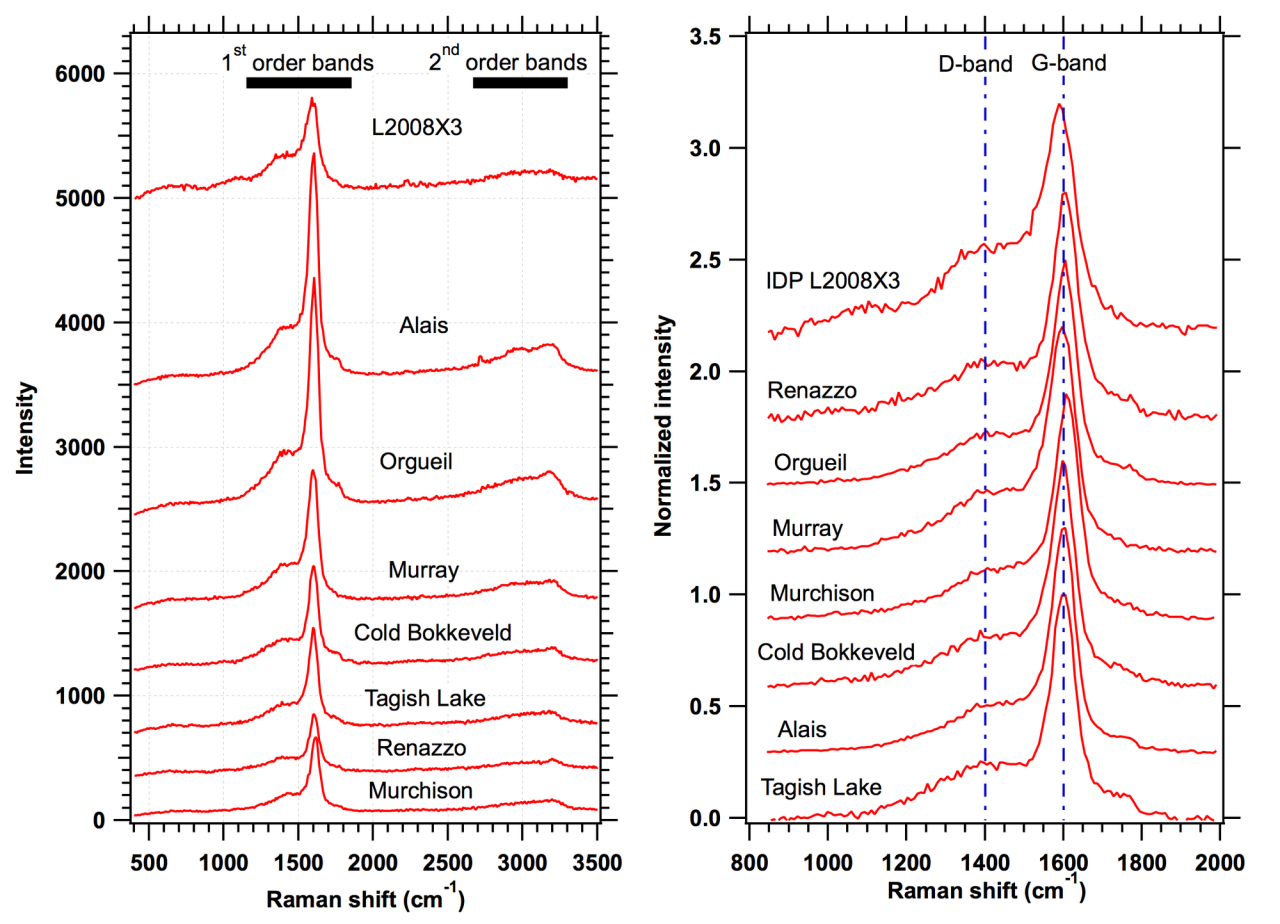
1st order bands
2nd order bands
L2008X3
Alais
Orgueil
Murray
Cold Bokkeveld
Tagish Lake
Renazzo
Murchison
Intensity
Raman shift (cm-1)
D-band
G-band
IDP L2008X3
Renazzo
Orgueil
Murray
Murchison
Cold Bokkeveld
Alais
Tagish Lake
Normalized intensity
Raman shift (cm-1)

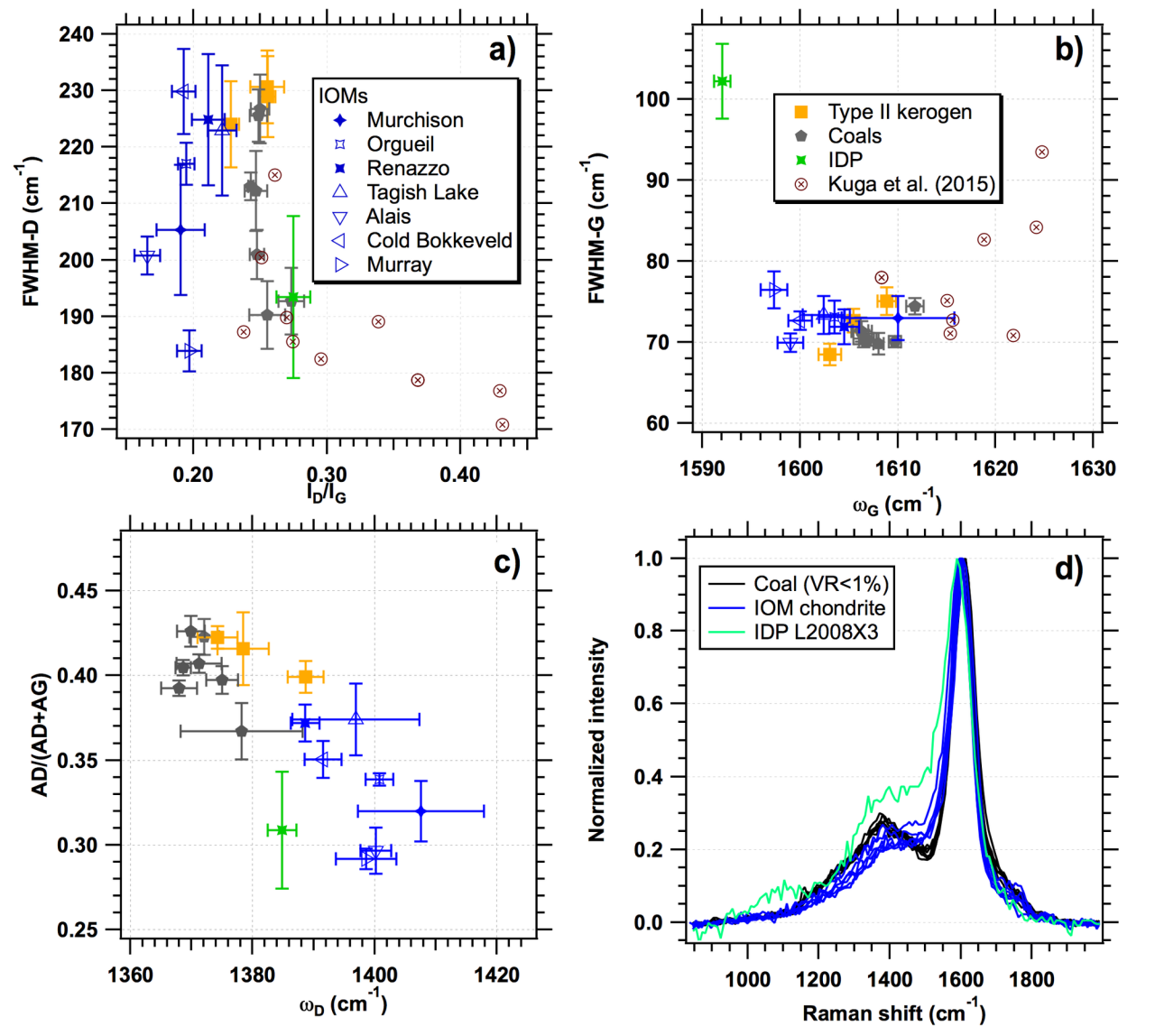
a)
IOMs
Murchison
Orgueil
Renazzo
Tagish Lake
Alais
Cold Bokkeveld
Murray
FWHM-D (cm-1)
ID/IG
b)
Type II kerogen
Coals
IDP
Kuga et al. (2015)
FWHM-G (cm-1)
ωG (cm-1)
c)
AD/(AD+AG)
ωD (cm-1)
d)
Coal (VR<1%)
IOM chondrite
IDP L2008X3
Normalized intensity
Raman shift (cm-1)

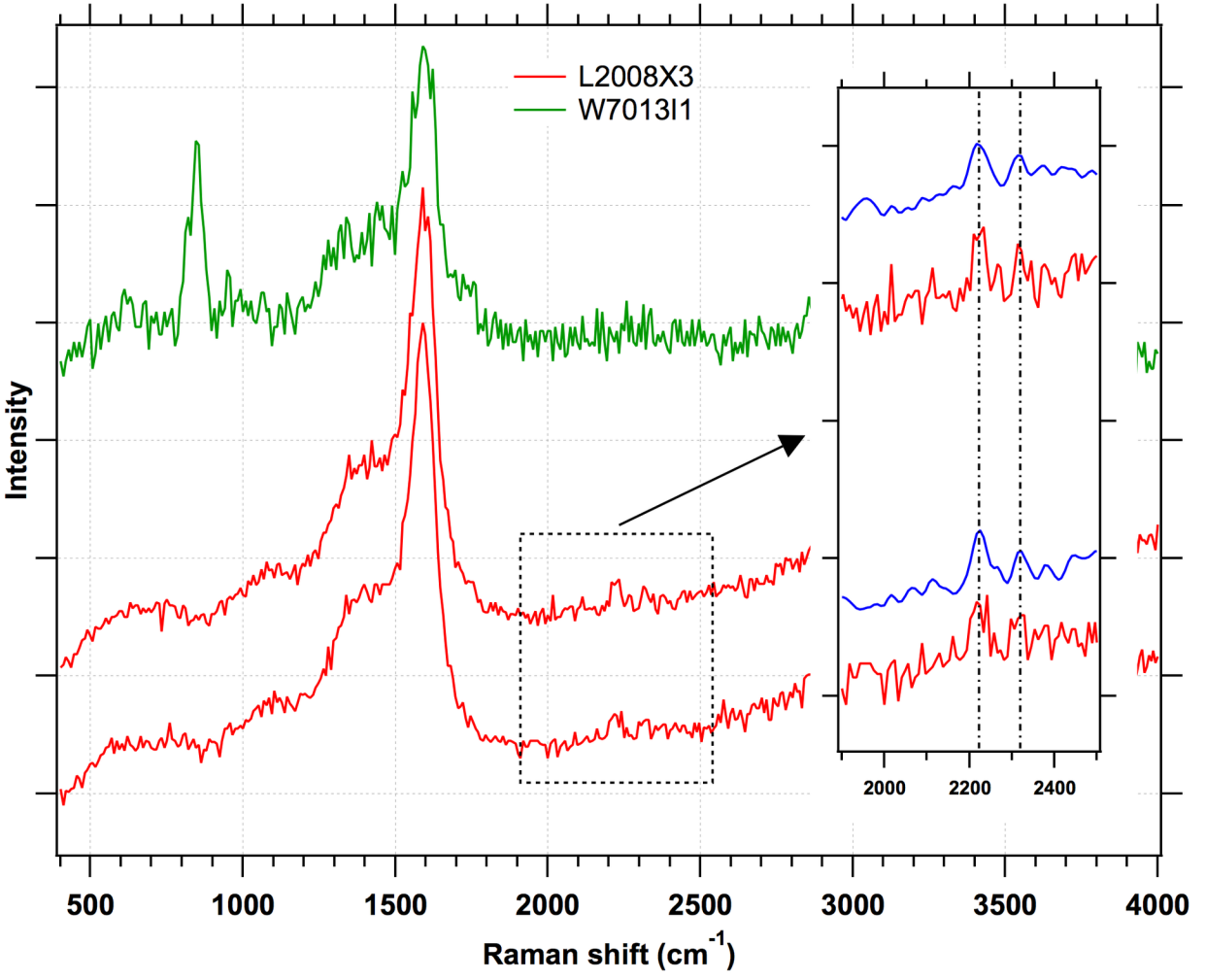
L2008X3
W7013I1
Intensity
500
1000
1500
2000
2500
3000
3500
4000
Raman shift (cm-1)
2000
2200
2400

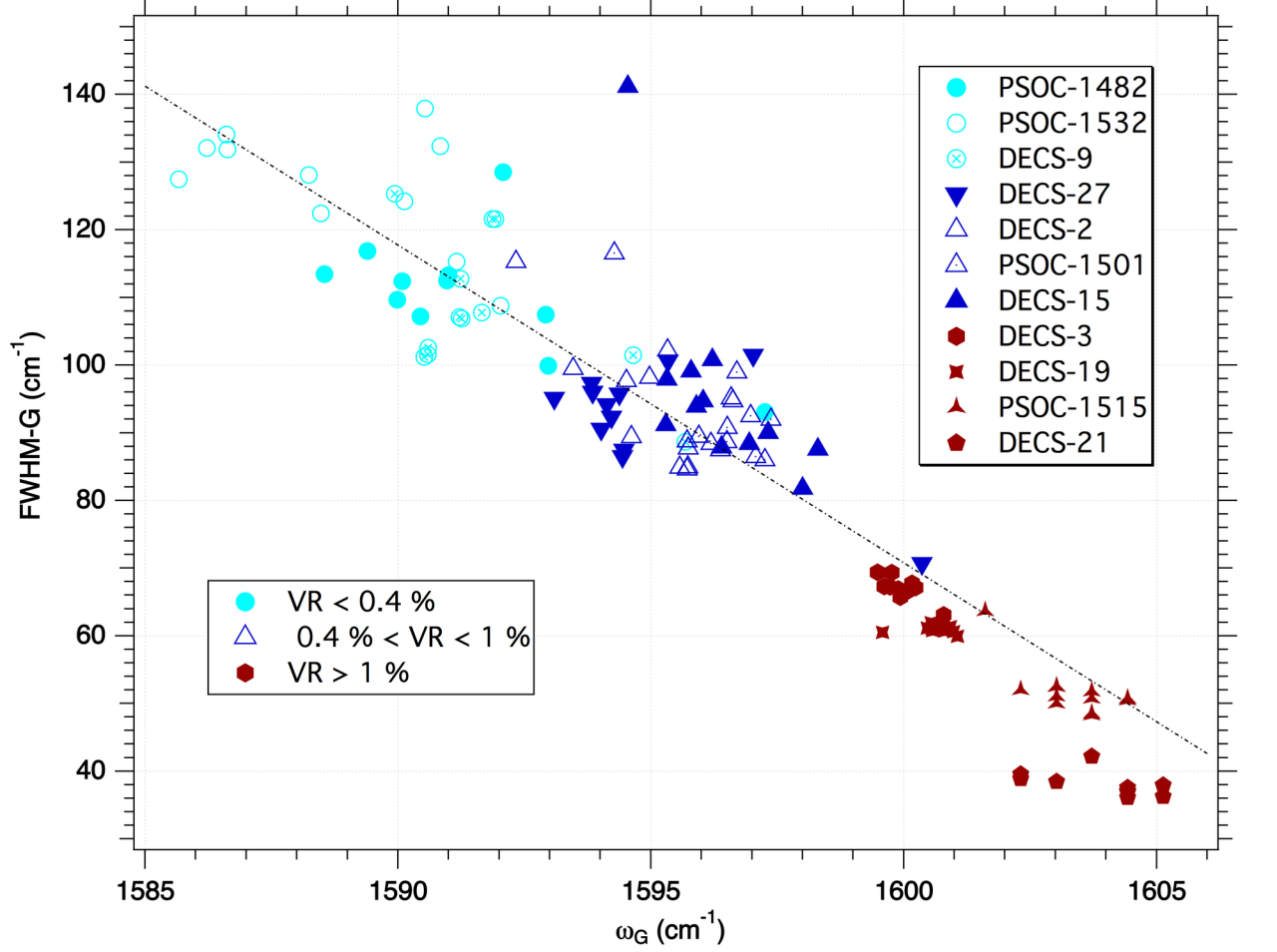
PSOC-1482
PSOC-1532
DECS-9
DECS-27
DECS-2
PSOC-1501
DECS-15
DECS-3
DECS-19
PSOC-1515
DECS-21
VR < 0.4 %
0.4 % < VR < 1 %
VR > 1 %
FWHM-G (cm-1)
ωG (cm-1)
140
120
100
80
60
40
1585
1590
1595
1600
1605

Table 1
Samples investigated.

Name	Sample/Class	R_O (%)	H/C	O/C
PSOC 1532	coal	0.33	0.90	0.25
DECS 11	coal	0.35	0.73	0.21
DECS 9	coal	0.38	0.82	0.17
PSOC 1482	coal	0.39	0.76	0.23
DECS 27	coal	0.46	0.82	0.13
DECS 2	coal	0.52	0.84	0.10
PSOC 1501	coal	0.73	0.79	0.11
DECS30	coal	1.16	0.73	0.038
PSOC 1540	coal	1.28	0.81	0.036
PSOC 1516	coal	1.73	0.63	0.026
PSOC 880	coal	1.86	0.66	0.020
PSOC 383	coal	2.57	0.54	0.023
PSOC 384	coal	2.7	0.50	0.012
PSOC 1515	coal	2.8	0.53	0.027
DECS 21	coal	5.19	0.53	0.029
K99296	Kerogen II		1.23	0.108
K20505	Kerogen II	0.57[a]	1.09	0.037
K20507	Kerogen II	1.25[a]	0.80	0.048
Orgueil[b]	CI		0.67	0.18
			0.72*	
Alais[b]	CI		0.72	0.15
Murchison[b]	CM		0.59	0.18
			0.70*	
Cold Bokkeveld[b]	CM (TII)		0.57	0.19
Murray[c]	CM (TII?)		0.68	0.17
Tagish Lake[b]	C2-ung (TII)			
Renazzo[c]	CR			
L2008x3[d]	IDP			
W7013I1	IDP			

The coal samples were provided by the Penn State University data bank. Type II kerogen samples were provided by Institut Français du Pétrole (Rueil-Malmaison, France). TII: heating stage according to Nakamura (2005) classification, estimated by Quirico et al. (2018). R_O: mean maximum reflectance of vitrinite, according to ADSTM classification (standard D-388). (a): allochthonous vitrinite. (b): spectra from Quirico et al. (2014), reanalyzed with a LBWF without constant (see text). (c): new IOM samples. (d): spectra from Dobrica et al. (2011), treated with a LBWF fit. H/C and O/C elemental ratio of Insoluble Organic Matter are from Alexander et al. (2007), except values tagged by a * mark that are from Gardinier et al. (2000). IDP: stratospheric Interplanetary Dust Particle.

Table 2
Spectral parameters from 244 nm Raman spectra

	Type	FWHM-G (cm^{-1})	ω_G (cm^{-1})	I_D/I_G	A_{DDG}	FWHM-D (cm^{-1})	ω_D (cm^{-1})
PSOC 1532*	coal	74.5 ± 1	1612 ± 1	0.27 ± 0.01	0.40 ± 0.01	193 ± 6	1375 ± 3
DECS 11		71 ± 2	1606 ± 1	0.25 ± 0.01	0.40 ± 0.01	201 ± 5	1368 ± 3
DECS 9		70.5 ± 1	1606.5 ± 1	0.24 ± 0.01	0.40 ± 0.01	213 ± 3	1369 ± 2
PSOC 1482		71.5 ± 2	1606 ± 1	0.24 ± 0.02	0.37 ± 0.02	190 ± 6	1378 ± 10
DECS27		70.5 ± 1	1607 ± 1	0.25 ± 0.01	0.41 ± 0.01	212 ± 7	1371 ± 4
DECS 2		70 ± 1	1610 ± 1	0.25 ± 0.01	0.43 ± 0.01	226 ± 5	1372 ± 3
PSOC 1501		70 ± 2	1608 ± 1	0.25 ± 0.01	0.43 ± 0.01	227 ± 6	1370 ± 3
PSOC 1532#		*68 ± 5*	*1605 ± 1*	*0.28 ± 0.02*	*0.48 ± 0.03*	*255 ± 37*	*1370 ± 1*
DECS 30		*61 ± 1*	*1607 ± 1*	*0.25 ± 0.01*	*0.50 ± 0.01*	*267 ± 3*	*1374 ± 6*
PSOC 1540		*62 ± 1*	*1606 ± 1*	*0.25 ± 0.01*	*0.50 ± 0.01*	*274 ± 6*	*1376 ± 4*
PSOC 1516		*58 ± 1*	*1608 ± 1*	*0.24 ± 0.01*	*0.47 ± 0.03*	*246 ± 23*	*1385 ± 7*
PSOC 880		*57 ± 2*	*1606 ± 1*	*0.20 ± 0.01*	*0.43 ± 0.04*	*244 ± 27*	*1399 ± 11*
PSOC 383		*57 ± 1*	*1607 ± 2*	*0.21 ± 0.02*	*0.45 ± 0.03*	*261 ± 8*	*1395 ± 9*
PSOC 384		*57 ± 2*	*1607 ± 1*	*0.22 ± 0.01*	*0.46 ± 0.02*	*256 ± 12*	*1393 ± 8*
PSOC 1515		*58 ± 1*	*1607 ± 1*	*0.22 ± 0.01*	*0.47 ± 0.02*	*271 ± 28*	*1393 ± 3*
DECS 21		*54 ± 1*	*1604 ± 2*	*0.16 ± 0.01*	*0.35 ± 0.02*	*233 ± 14*	*1432 ± 8*
K99296	kerogen II	75 ± 2	1609 ± 1	0.25 ± 0.01	0.42 ± 0.02	231 ± 7	1378 ± 4
K20505		73 ± 2	1605.5 ± 1	0.26 ± 0.01	0.43 ± 0.01	229 ± 7	1374 ± 4
K20507		68.5 ± 2	1603 ± 2	0.23 ± 0.01	0.40 ± 0.01	224 ± 8	1389 ± 3
Orgueil	CI1	73 ± 2	1604 ± 2	0.19 ± 0.01	0.34 ± 0.01	217 ± 4	1401 ± 3
Alais	CI1	70 ± 2	1599 ± 2	0.17 ± 0.01	0.30 ± 0.02	201 ± 8	1400 ± 3
Murchison	CM2	73 ± 3	1610 ± 6	0.19 ± 0.02	0.32 ± 0.02	205 ± 12	1408 ± 10
Cold Bokkeveld	CM2 [TII]	73 ± 1	1600 ± 2	0.19 ± 0.01	0.35 ± 0.01	230 ± 8	1391 ± 3
Murray	CM2 [TII ?]	76.5 ± 3	1597 ± 2	0.20 ± 0.01	0.29 ± 0.01	184 ± 4	1399 ± 5
Tagish Lake	C2-ung [TII]	73.5 ± 3	1602 ± 3	0.22 ± 0.01	0.37 ± 0.02	223 ± 12	1397 ± 10
Renazzo	CR2	72 ± 2	1604 ± 2	0.21 ± 0.01	0.37 ± 0.01	225 ± 12	1389 ± 3
L2008x3	IDP	102 ± 5	1592 ± 1	0.27 ± 0.01	0.31 ± 0.04	193 ± 15	1385 ± 3

Immature coals (Ro<1%), collected with P=300 µW on the sample, 2x150 s and 600 gr/mm grating. * Mature coals (Ro>1%), collected with P=500 µW, 2x300 s and 3600 gr/mm grating (in italic in the table). All samples fitted with a LBWF model without constant (see text).

Table 3
Spectral parameters from 514 nm Raman spectra (Bonal et al., 2011)

	FWHM-G (cm^{-1})	**ω_G (cm^{-1})**	**I_D/I_G**	**FWHM-D (cm^{-1})**	**ω_D (cm^{-1})**
L2008x3	125.3 ± 3.8	1575.7 ± 2.7	1.03 ± 0.04	294.7 ± 17.2	1359.3 ± 2
W7013I1	108.5 ± 6.9	1686.5 ± 2.3	1.03 ± 0.04	235.2 ± 10.1	1359.6 ± 2.3